

DOI: 10.1093/jcde/gwaf071

Advance access publication date: 23 July 2025 Research Article

Computational modelling and sensitivity analysis of heat transfer in ternary nanofluids using response surface methodology

Sami Ul Haq ¹⁰1, Muhammad Bilal Ashraf ¹⁰1, Arooj Tanveer ¹⁰1, Jongsuk Ro ¹⁰2,3,*, Fuad A. Awwad ¹⁰4 and Emad A. A. Ismail ¹⁰4

Abstract

This study investigates the thermal optimization of ternary nanofluids, especially focusing on sensitivity analysis of the physical parameters. This study provides an efficient thermal management system that is essential in sophisticated cooling systems, such as electric vehicle battery packs and aerospace engines, to avoid overheating and maintain uniform temperature distribution. A statistical approach is used to analyze the skin friction and heat transfer rate via Response Surface Methodology and Analysis of Variance. Furthermore, irreversibility analysis is also calculated, arising due to Joule heating and viscous dissipation. A non-similar transformation is used to convert the boundary layer equations into dimensionless partial differential equations. The system of partial differential equations is converted into an ordinary differential equation using a local non-similar method up to second-order truncation. These systems of ordinary differential equations are solved numerically via bvp4c. Sensitivity analysis is performed for drag force and heat transfer rate for input parameters. The correlations between input factors and output responses are created via the use of analysis of variance tables, which is beneficial for regression analysis. The high values of $R^2 = 99.84\%$, $R^2(Adj) = 99.70\%$ for drag force and $R^2 = 99.97\%$, $R^2(Adj) = 99.94\%$ for heat transfer rate show that high validity of analysis of variance results is obtained to perform sensitivity analysis. The results conclude that the Hartmann number is the most impactful factor among other parameters for friction and heat transfer rate at the surface. The Eckert number and volume fraction coefficient are caused to rise in entropy generation.

Keywords: ternary nanofluids, entropy generation, sensitivity analysis, RSM, ANOVA

Nomenclature

 $\begin{array}{lll} \textit{v}, \textit{s}: & \textit{Velocity components } [\textit{ms}^{-1}] \\ \textit{r}, \textit{s}: & \textit{Curvilinear coordinates } [\textit{m}] \\ \textit{a}: & \textit{Stretching constant } [\textit{s}^{-1}] \\ \textit{\mu}: & \textit{Dynamic viscosity} [\textit{Kg m}^{-1} \textit{s}^{-1}] \\ \textit{\rho}: & \textit{Fluid density } [\textit{Kg m}^{-3}] \\ \textit{h}: & \textit{Convective heat transfer} \end{array}$

 C_p : Specific heat

 k_f : Thermal conductivity [w mk⁻¹]

R: Radius [m]

p: Pressure [kg m⁻¹ s⁻²] P: Dimensionless pressure

k: Dimensionless curvature parameter ν : Kinematics viscosity [m 2 s $^{-1}$] T_{∞} : Ambient fluid temperature [K]

 T_f : Wall temperature

 $(\rho C)_f$: Heat capacity of fluid $[j kg^{-1} K^{-1}]$

B: Applied magnetic field σ : Electric conductivity [S m⁻¹]

L: Slip length

1. Introduction

Park et al. (2025) optimized the uniform temperature distribution in an electric vehicle (EV) liquid-cooled cylindrical lithiumion battery utilizing a kriging metamodel and covariance matrix adaptation evolution strategy (CMA-ES). Alqahtani et al. (2024) discussed the sensitivity analysis of the lithium-ion battery model using the Osprey optimization algorithm. Alrashdan et al. (2024) optimized the charging of lithium-ion batteries using the Taguchi method. Zeng et al. (2025) optimized the dielectric coolants in EV batteries using data-driven and computational fluid dynamics (CFD) approaches. Li et al. (2024) optimized the efficiency of lithium-ion batteries using CFD and artificial neural network (ANN) approaches. Sensitivity analysis is a crucial problem that is used to investigate the impact of numerous input parameters on a variety of flow complexities in the fields of engineering and manufacturing industries. In order to find the best control systems, sensitivity analysis is now utilized extensively in engineering and industry. The concept of sensitivity analysis, which involves examining the impact of changes in physical systems, has been applied to several scientific and technological fields, such as

¹Department of Mathematics, COMSATS University Islamabad (CUI), 45550 Park Road, Tarlai Kalan, Islamabad, Pakistan

²School of Electrical and Electronics Engineering, Chung-Ang University, Dongjak gu, Seoul 06974, Republic of Korea

³Department of Intelligent Energy and Industry, Chung-Ang University, Dongjak gu, Seoul 06974, Republic of Korea

⁴Department of Quantitative Analysis, College of Business Administration, King Saud University, PO Box 71115, Riyadh 11587, Saudi Arabia

^{*}Correspondence: jsro@cau.ac.kr

industrial production, nuclear engineering, ecology, biology, and socioeconomics. Sensitivity analysis necessitates the construction of an empirical correlation between the dependent and independent variables. Sensitivity analysis provides the optimal solution in different engineering and industrial processes. It provides an optimal relationship between the various factors and their impacts on the system behaviours, which produces the durable design, reduces the failure of experiments, and promotes costeffective decision-making by stressing areas. Effective thermal management of EV battery packs is essential to avert overheating, which diminishes performance and limits lifespan. Conventional cooling techniques frequently fail to attain uniform temperature distribution within battery cells. Increasing the thermal conductivity and specific heat capacity of ternary nanofluids helps control friction and heat transfer rates. Many researchers use this methodology in fluid flow problems. Hossain et al. (2023) discussed the magnetohydrodynamics (MHD) flow of Bingham nanofluids filled with a wavy cavity using the finite-volume method and sensitivity analysis. Priyadharsini et al. (2023) provide the sensitivity analysis of unsteady transport phenomena of blood flow in arteries in the presence of chemical reactions. Areekara et al. (2023) examined the importance of nanoparticles in the Casson fluid flow under electromagnetic hydrodynamics. Farooq et al. (2024) provided the numerical solution of hybrid nanofluids over a cylinder with the Cattaneo-Christov heat flux model.

Aldandani et al. (2025) provided the non-similar solution to enhance the thermal energy of Reiner-Philippoff nanofluids over curved geometry using neural computing. Akbar et al. (2024) discussed the quadratic convection phenomena of Carreau-Yasuda fluid with variable thermal properties. Joshi et al. (2025) analysed the entropy production in lithium-ion batteries with a porous medium. Xiong et al. (2024) analysed the magneto-sensitive shear thickening fluid based on multi-functional battery modules' heat control and antimechanical abuse. Mustafa et al. (2023) provided the numerical solution of the two-phase flow of turbulent nanofluids in circular heatsinks with entropy generation. Entropy generation is the most important fluid flow phenomenon that affects the efficiency of thermal and fluidic systems. Entropy generation means the irreversibility within the fluidic system that arises due to the viscous dissipation, Joule heating, and heat transfer, which reduce the quality of energy and efficiency in the system. Higher entropy production indicates a high rate of energy consumption, inefficiency, and worse system performance. Researchers focus on analysing and minimizing the entropy generation to increase sustainability, minimize the energy lost, and design a more optimal and efficient system. Minimization of entropy generation within the system is critical for optimization processes and has a variety of applications, such as power generation, cooling systems, hydraulic systems, reducing drag in vehicles, and overall improving the energy performance within the systems. Nagaraja et al. (2023) discussed the ANOVA (analysis of variance)-Taguchi technique to optimize the heat transfer rate of Prandtl nanofluids with entropy generation. Analysing the entropy production of Casson fluid with the effect of Joule heating using a non-similar approach was covered by Louati et al. (2024). Zhang et al. (2024) provided the unsteady flow of Casson fluid across a stretching plate with their irreversibility analysis. Mondal et al. (2020) computationally analysed the impact of variable viscosity nanofluid flow over a non-linear stretching surface with gyrotactic microorganisms.

Fayz-Al-Asad et al. (2024) discussed the thermal enhancement in the undulating wavy cavity of a cylinder utilizing the FEM. Wang et al. (2023) improve the thermal performance by incorporating hybrid nanofluid through a rotatory porous cone. Venkateswarlu et al. (2025) provided the computational study on the improvement of cooling in lithium-ion batteries using hybrid nanofluids. Liao et al. (2022) studied the thermal performance of lithium-ion batteries utilizing copper-water-based nanofluids. Bayareh et al. (2023) discussed the two-phase flow of nanofluids in macro- and microchannels with non-Newtonian fluids. Nanofluids are dilute liquids that have tiny particles dispersed throughout them. The nanoparticles utilized in nanofluids are typically composed of metals, oxides, carbides, or carbon nanotubes, while the usual base fluids include water, ethylene glycol, and oil. Nevertheless, the previously mentioned common base fluid exhibits a limited ability to improve the thermal conductivity of the fluid. Therefore, a different approach has been developed by incorporating nanoparticles into the base fluid. The reason for this is that the interaction of nanoparticles within the base fluid represents an effective method to improve the thermal conductivity of the fluid. The researcher states that incorporating a small amount (< 1% volume fraction) of nanoparticles into the base fluid can improve thermal conductivity. This is due to the fact that nanometre-sized nanoparticles behave like fluid molecules, which will boost heat conductivity. Nanoparticles of Al₂O₃, Cu, and TiO₄ are commonly used in nanofluids and have well-known thermophysical properties. These nanoparticles have exceptional thermal conductivity and stability, making them suitable for improving heat transfer across many applications. The Al₂O₃ and TiO₂ are considered for superior thermal conductivity and low cost, whilst Cu has excellent thermal performance. Ouyang et al. (2024) studied the stability analysis of Maxwell ternary nanofluids across a stretching surface. Madkhali et al. (2023) discussed the transport of Carreau-Yasuda ternary nanofluids with the Cattaneo-Christov heat flux model using the finite-element method (FEM). Zhang et al. (2021) discussed the convective flow of stagnation point nanofluids over a curved stretching surface with a Joule heating effect. Hosseinzadeh et al. (2022) investigate MHD transport of second-grade viscoelastic fluid with nanofluids over a curved stretching surface. Aly et al. (2019) provide efficient numerical and analytical solutions of hybrid nanofluids in a porous medium subject to connective boundary conditions. Rao & Deka (2023) analysed the bioconvection transport of hybrid nanofluids with motile microorgan-

Vahedi et al. (2018) optimized the MHD flow around a porous cylinder using response surface methodology (RSM). Dwidmuthe et al. (2020) discussed the blood flow phenomena in stenotic arteries using RSM to predict the pressure drops. Micropolar fluid flow in a channel subjected to thermal radiation and a magnetic field with sensitivity analysis by Alahmadi et al. (2023). Esfe et al. (2022) predicted the rheological behaviour of hybrid nanolubricant using RSM. Rana et al. (2023) analysed the stability of non-Newtonian fluid with slip and convective boundary condition. RSM is an important technique to optimize the complex fluid flow problem with different parameters. RSM provides optimum conditions of the physical quantities, such as flow uniformity, heat transfer rate, and pressure control for the different parameters of utilizing the statistical approach. Experiment design is a crucial part of industrial and engineering processes. RSM is a very popular optimization experiment that employs statistics and mathematics to calculate the optimal solution by analysing the impact of different parameters on the responses. ANOVA is used to check if the generated model of RSM is accurate. To find the exact mechanism and determine the parameter values that optimize the response, the RSM is a helpful technique. RSM has now been studied with a hybrid design model that combines face-centred and full

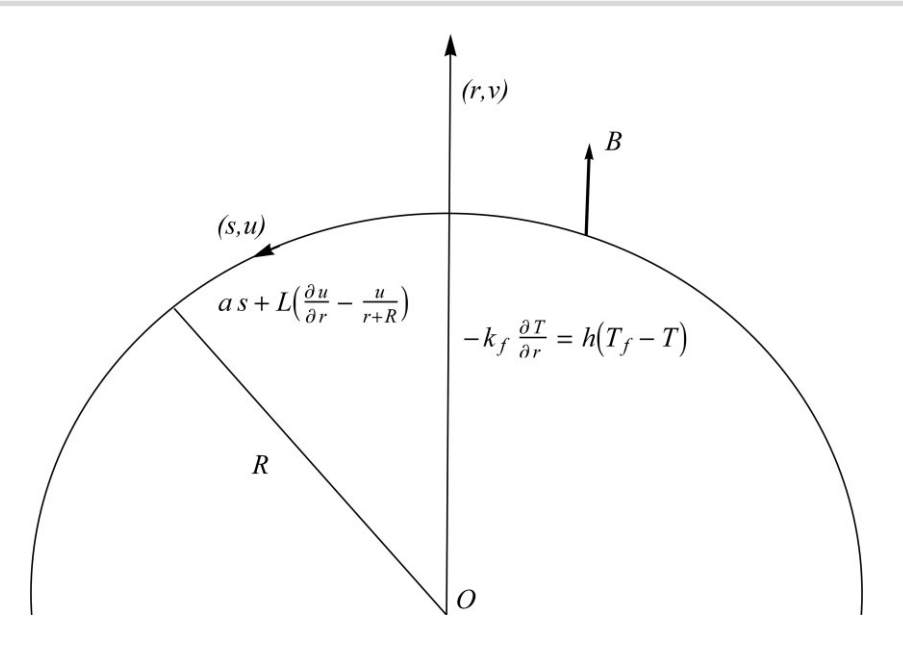


Figure 1: Geometry of the problem.

factorial approaches. Khashi et al. (2022) employed a statistical method to examine the rate of heat transfer and skin friction in hybrid nanofluids flowing over a permeable wedge. Geng et al. (2024) used RSM to find the optimal solution of a cross-flow water turbine in a circular cavity. Yang et al. (2023) used a central composite design (CCD) to perform novel-type vortex generator structures via RSM. Richa et al. (2024) discussed the minimization of entropy generation in nanofluids flowing over a porous surface with the Koo-Kleinstreuer-Li approach. For heat transfer analysis of non-Newtonian fluid (Ullah & Ashraf, 2024a,b; Iqbal & Abbasi, 2024; Mehmood et al., 2024; Ul-Haq & Mehmood, 2024; Alkinidri et al., 2025; Mehmood & Rehman, 2025).

The similar solution of the ternary nanofluids flowing over a curved surface with viscous dissipation has been studied by many researchers. In this study, we discussed the non-similar solution of ternary nanofluids flowing over a curved stretching surface with irreversibility analysis. The basic aim of this study is to find the optimal value among several physical parameters for skin friction and local Nusselt number. In this regard, we performed the sensitivity analysis utilizing a CCD grounded on RSM. A non-similar solution is found up to second-order truncations and solved numerically using Bpv4c. The first novelty of this problem comes from the non-similar solution of ternary nanofluids flowing over a curved surface with irreversibility analysis. Secondly, the statistical method of RSM is used to perform sensitivity of the physical parameters for the heat transfer rate and the drag force. The aforementioned problem has not yet been studied and published. This research seeks to improve the efficiency of engineering problems by evaluating the impact of different parameters on cost. The following research questions are discussed in our study.

- Why is the local non-similar solution important?
- What is the effect of a ternary fluid over a curved surface in the presence of viscous dissipation?
- · How do ternary nanofluids react in the conducting fluid over a curved stretching surface?
- How does the Bejan number minimize the entropy generation of ternary nanofluids flowing under viscous dissipation and Joule heating effects?

- Which parameters are most influential that affect the friction and heat transfer at the surface?
- How are responses (skin friction and Nusselt number) affected by the independent variables?

2. Mathematical Formulation

Figure 1 illustrates the 2D, incompressible transport of ternary nanofluids over a curved stretching surface subjected to an externally supplied magnetic field. The momentum and energy equations are formulated via curvilinear coordinates. The sphereshaped nanoparticles of aluminum oxide, copper oxide, and titanium dioxide are considered to be suspended in a base fluid, e.g., water. The slip velocity and convective boundary condition are taken into account in this problem. Let v and u are velocity components considered r- and s-directions, while axial velocity is stretched in the s-direction. In this problem, the viscous dissipation and Joule heating effects are assumed in the energy equation. The continuity, momentum, and energy equations are defined as

$$\nabla . V = 0 \tag{1}$$

$$\rho (V.\nabla) V = -\nabla p + \nabla . V + J \times B$$
 (2)

$$(\rho C_p)(v.\nabla)T = k\nabla^2 T + \tau.L + \frac{1}{\sigma}JJ$$
(3)

The vector X is defined for the curved surface coiled in a circular form of radius R as

$$X = \left((r + R) \cos \left(\frac{s}{R} \right), (r + R) \sin \left(\frac{s}{R} \right), z \right) \tag{4}$$

The del operator for a curved surface is defined as

$$\nabla = \frac{\partial}{\partial r} + \frac{r + R}{R} \frac{\partial}{\partial s} + \frac{\partial}{\partial z}$$
 (5)

For the boundary layer's equation for a curved surface, we introduce the following dimensionless variables:

$$\mathbf{s}^* = \frac{\mathbf{s}}{\mathbf{L}}, \ \mathbf{r}^* = \frac{\mathbf{r}}{\varepsilon}, \mathbf{R}^* = \frac{\mathbf{R}}{\varepsilon}, \ \mathbf{u}^* = \frac{\mathbf{u}}{U_0}, \mathbf{v}^* = \frac{\mathbf{v}}{U_0} \frac{\mathbf{L}}{\varepsilon}, \ \mathbf{p}^* = \frac{\mathbf{p}}{\rho U_0^2} \tag{6}$$

Using Equations 4-6 in Equations 1-3, we get the boundary layer equations that are given below in equations

Table 1: The properties of tri-nanofluids (Ramzan et al., 2023) are given below.

Physical properties	Tri nanofluid
Viscosity (μ)	$\mu_{ ext{tnf}} = rac{\mu_{ ext{H}_2 ext{O}}}{(1 - arphi_{ ext{A}_2 ext{O}_3})^{2.5} (1 - arphi_{ ext{H}_2 ext{O}}} (1 - arphi_{ ext{H}_2 ext{O}_3})^{2.5}}$
Density (ho)	$\rho_{\rm tnf} = (1 - \varphi_{\rm TiO_2})[(1 - \varphi_{\rm CuO})\{(1 - \varphi_{\rm Al_2O_3})\rho_{\rm H_2O} + \varphi_{\rm Al_2O_3}\rho_{\rm Al_2O_3}\} + \varphi_{\rm CuO}\rho_{\rm CuO}] + \varphi_{\rm TiO_2}\rho_{\rm TiO_2}$
Heat capacity (ρC_p)	$(\rho C_p)_{\rm tnf} = (1 - \varphi_{\rm TiO_2})[(1 - \varphi_{\rm CuO})\{(1 - \varphi_{\rm Al_2O_3})(\rho C_p)_{\rm H_2O} + \varphi_{\rm Al_2O_3}(\rho C_p)_{\rm Al_2O_3}\} \\ + \varphi_{\rm CuO}(\rho C_p)_{\rm CuO}] + \varphi_{\rm TiO_2}(\rho C_p)_{\rm TiO_2} + \varphi_{\rm Al_2O_3}(\rho C_p)_{\rm Al_2O_3}\} \\ + \varphi_{\rm CuO}(\rho C_p)_{\rm CuO} + \varphi_{\rm TiO_2}(\rho C_p)_{\rm TiO_2} + \varphi_{\rm Al_2O_3}(\rho C_p)_{\rm Al_2O_3}\} \\ + \varphi_{\rm CuO}(\rho C_p)_{\rm CuO} + \varphi_{\rm TiO_2}(\rho C_p)_{\rm TiO_2} + \varphi_{\rm Al_2O_3}(\rho C_p)_{\rm Al_2O_3}\} \\ + \varphi_{\rm CuO}(\rho C_p)_{\rm CuO} + \varphi_{\rm TiO_2}(\rho C_p)_{\rm TiO_2} + \varphi_{\rm Al_2O_3}(\rho C_p)_{\rm Al_2O_3}\} \\ + \varphi_{\rm CuO}(\rho C_p)_{\rm CuO} + \varphi_{\rm TiO_2}(\rho C_p)_{\rm TiO_2} + \varphi_{\rm Al_2O_3}(\rho C_p)_{\rm Al_2O_3}\} \\ + \varphi_{\rm CuO}(\rho C_p)_{\rm CuO} + \varphi_{\rm Al_2O_3}(\rho C_p)_{\rm CuO} + \varphi_{\rm Al_2O_3}$
Thermal conductivity (k)	$k_{tnf} = k_{hnf}(\frac{(k_{\Pi O_2} + 2k_{lnf}) - \varphi_{\Pi O_2}(k_{lnf} - k_{\Pi O_2})}{(k_{\Pi O_2} + 2k_{lnf}) + \varphi_{\Pi O_2}(k_{lnf} - k_{\Pi O_2})})k_{hnf} = k_{nf}(\frac{(k_{ClO} + 2k_{nf}) - \varphi_{ClO}(k_{nf} - k_{ClO})}{(k_{ClO} + 2k_{nf}) + \varphi_{ClO}(k_{nf} - k_{ClO})})k_{nf} = k_{f}(\frac{(k_{Al_2 O_3} + 2k_{lh_2 O}) - \varphi_{Al_2 O_3}(k_{lh_2 O} - k_{Al_2 O_3})}{(k_{Al_2 O_3} + 2k_{lh_2 O}) + \varphi_{Al_2 O_3}(k_{lh_2 O} - k_{Al_2 O_3})})$
Electrical conductivity (σ)	$\sigma_{\rm tnf} = \sigma_{hnf}(\frac{\sigma_{\rm TiO_2}(1+2\varphi_{\rm TiO_2})+\sigma_{hnf}(1-2\varphi_{\rm TiO_2})}{\sigma_{\rm TiO_2}(1-\varphi_{\rm TiO_2})+\sigma_{hnf}(1+\varphi_{\rm TiO_2})})\sigma_{hnf} = \sigma_{nf}(\frac{\sigma_{\rm CiO}(1+2\varphi_{\rm CiO})+\sigma_{nf}(1-2\varphi_{\rm CiO})}{\sigma_{\rm CiO}(1-\varphi_{\rm CiO})+\sigma_{nf}(1+\varphi_{\rm CiO})})\sigma_{nf} = \sigma_{f}(\frac{\sigma_{Al_2O_3}(1+2\varphi_{Al_2O_3})+\sigma_{hg_2O}(1-2\varphi_{Al_2O_3})}{\sigma_{Al_2O_3}(1-\varphi_{Al_2O_3})+\sigma_{hg_2O}(1+\varphi_{Al_2O_3})})$

Table 2: Thermophysical characteristics of nanofluids (Devi, 2024) are given below.

Thermophysical properties	H ₂ O	Al_2O_3	CuO	TiO ₂
$C_p \ (J \ kg^{-1} \ K^{-1})$	4179	765	5315	686.2
ρ (kg m ⁻³)	997.1	3970	6320	4250
$k (w mK^{-1})$	0.613	40	76.5	8.9538
$\sigma (\mathrm{S} \mathrm{m}^{-1})$	5.5×10^{-6}	1×10^{-10}	2.7×10^{-8}	6.27×10^{-5}

The modelled equations (Ul-Haq et al., 2023) related to the problem are

$$\frac{\partial}{\partial r} \left[(r + R) v \right] + R \frac{\partial u}{\partial s} = 0 \tag{7}$$

$$-\frac{u^2}{r+R} = -\frac{1}{\rho_{\rm tnf}} \frac{\partial p}{\partial r} \tag{8}$$

$$v\frac{\partial u}{\partial r} + \frac{Ru}{r+R}\frac{\partial u}{\partial s} + \frac{uv}{r+R} = -\frac{1}{\rho_{\text{tnf}}}\frac{R}{r+R}\frac{\partial p}{\partial s} + \frac{\mu_{\text{tnf}}}{\rho_{\text{tnf}}}$$

$$\times \left(\frac{\partial^{2} u}{\partial r^{2}} + \frac{1}{r+R} \frac{\partial u}{\partial r} - \frac{u}{(r+R)^{2}} \right) - \frac{\sigma_{\text{tnf}} R^{2} B^{2} u}{\rho_{\text{tnf}} (r+R)^{2}}$$
(9)
$$\left(\rho C_{p} \right)_{\text{tnf}} \left(v \frac{\partial T}{\partial r} + \frac{Ru}{r+R} \frac{\partial T}{\partial s} \right) = k_{\text{tnf}} \left(\frac{\partial^{2} T}{\partial r^{2}} + \frac{1}{r+R} \frac{\partial T}{\partial r} \right)$$

$$+\mu_{\rm tnf} \left(\frac{\partial u}{\partial r} - \frac{u}{r+R}\right)^2 + \frac{\sigma_{\rm tnf} R^2 B^2 u^2}{(r+R)^2}$$
 (10)

Here, $k_{\rm tnf}$, $\sigma_{\rm tnf}$, B, p, $\rho_{\rm tnf}$, T_{∞} , $(C_p)_{\rm tnf}$, and $\mu_{\rm tnf}$ represent the thermal conductivity of ternary nanofluids, electrical conductivity of ternary nanofluids, applied magnetic field, pressure, density of ternary nanofluids, ambient temperature, heat capacity, and heat dynamics viscosity of ternary nanofluids, respectively. Ternary nanofluids are applicable only to Newtonian (viscous) fluids and are not suitable for non-Newtonian fluids because the thermophysical properties have been primarily derived for Newtonian behaviour. Ensuring a stable solution with a homogeneous dispersion of nanoparticles in the base fluid remains a significant challenge. Additionally, the addition of nanoparticles increases the viscosity of the base fluid, which lead to higher pumping energy requirements and pressure drops in the system. Tables 1 and 2 provide the expression and experimental values of the thermophysical properties of ternary nanofluids.

The boundary conditions (Haq et al., 2023) of the problem are

$$u = as + L\left(\frac{\partial u}{\partial r} - \frac{u}{r+R}\right), v = 0, -k_f \frac{\partial T}{\partial r} = h\left(T_f - T\right) \text{ at } r = 0$$

$$u \to 0, \frac{\partial u}{\partial r} \to 0, T \to T_\infty \text{atr} \to \infty$$
(11)

The flow is induced due to continuous stretching of the surface. The condition $u = as + L(\frac{\partial u}{\partial r} - \frac{u}{r+R})$ represents axial stretching velocity with a slip component controlled by L. The condition v=0implies no radial flow, restricting motion to the axial direction. The heat flux condition $-k_f \frac{\partial T}{\partial r} = h(T_f - T)$ represents convective heat transfer between the fluid and the surface, where the left-hand side of the equation is due to the Fourier law of heat conduction, while the right-hand side is Newton's Law of cooling. As $r \to \infty$, the velocity $u \to 0$ and $\frac{\partial u}{\partial r} \to 0$ approaches zero, indicates that the flow becomes quiescent far from the surface along with the temperature approaching ambient temperature $T \to T_{\infty}$.

The non-similar transformation is given below

$$u(\hat{\xi}, \eta) = as \frac{\partial f(\hat{\xi}, \eta)}{\partial \eta}, \quad v(\hat{\xi}, \eta) = -\frac{R}{r + R} \sqrt{av_f} \left(f(\hat{\xi}, \eta) + \hat{\xi} \frac{\partial f(\hat{\xi}, \eta)}{\partial \hat{\xi}} \right),$$

$$p = \rho_f a^2 s^2 P(\hat{\xi}, \eta), \quad \theta(\hat{\xi}, \eta) = \frac{T - T_{\infty}}{T_f - T_{\infty}}, \quad \hat{\xi} = \frac{s}{L}, \quad \eta = \sqrt{\frac{a}{v_f}} r$$

$$(12)$$

By using Equations 12, Equations 8-10 are given as:

$$\frac{\partial P}{\partial \eta} = F_{1} \frac{f'^{2}}{\eta + k}$$

$$\frac{1}{F_{1}} \left(\frac{2kP}{\eta + k} + \hat{k} \frac{k}{\eta + k} \frac{\partial P}{\partial \hat{k}} \right) = \frac{1}{F_{1}F_{2}} \left(f''' + \frac{f''}{\eta + k} - \frac{f'}{(\eta + k)^{2}} \right)$$

$$+ \frac{1}{\eta + k} \left(kff'' - kf'^{2} + \frac{kff'}{\eta + k} \right)$$

$$+ \hat{k} \frac{k}{\eta + k} \left(f'' \frac{\partial f}{\partial \hat{k}} - f' \frac{\partial^{2} f}{\partial \eta \partial \hat{k}} + \frac{1}{\eta + k} f' \frac{\partial f}{\partial \hat{k}} \right)$$

$$- \frac{F_{5}}{F_{1}} \frac{k^{2}}{(\eta + k)^{2}} M^{2} f'$$

$$\frac{F_{4}}{F_{3}} \left(\theta'' + \frac{1}{\eta + k} \theta' \right) + Pr \frac{k}{\eta + k} f \theta' + \hat{k} Pr \frac{k}{\eta + k} \left(\theta' \frac{\partial f}{\partial \hat{k}} - f' \frac{\partial \theta}{\partial \hat{k}} \right)$$

$$+ \hat{k}^{2} Br \frac{1}{F_{2}F_{3}} \left(f'' - \frac{f'}{\eta + k} \right)^{2} + \hat{k}^{2} Br \frac{F_{5}}{F_{3}} \frac{k^{2}}{(\eta + k)^{2}} M^{2} f'^{2} = 0$$
(15)

$$f'(\hat{\xi},0) = 1 + \alpha \left(f''\left(\hat{\xi},0\right) - \frac{f'}{\eta + k} \right), \ f\left(\hat{\xi},0\right) + \hat{\xi} \frac{\partial f}{\partial \hat{\xi}} \left(\hat{\xi},0\right) = 0,$$

$$\theta'\left(\hat{\xi},0\right) = -\gamma_1 \left(1 - \theta\left(0\right)\right) \ f'\left(\hat{\xi},\infty\right) \to 0,$$

$$f''\left(\hat{\xi},\infty\right) \to 0, \ \theta\left(\hat{\xi},\infty\right) \to 0$$
(16)

Here, $\mathbf{k}=\mathbf{R}\sqrt{\frac{a}{\upsilon_f}}$ is the curvature parameter, $\alpha=\mathbf{L}\sqrt{\frac{a}{\upsilon_f}}$ is the velocity slip parameter, $\Pr = \frac{\mu_f(\mathbf{c_p})_f}{k_f}$ the Prandtl number, $\gamma_1 = -\frac{h\sqrt{v}}{k_f\sqrt{a}}$ the Biot number, $\Pr = \operatorname{Ec} \Pr = \frac{\mu_f a^2 L^2}{k_f(T-T_\infty)}$ the Brinkman parameter, and $M^2 = \frac{\sigma_f B^2}{a \, \rho_f}$ the Hartmann parameter.

$$arphi_{
m Al_2O_3} = arphi_{
m CuO} = arphi_{
m TiO_2} = arphi$$

$$\begin{split} F_{1} &= \left(1 - \varphi_{\text{TiO}_{2}}\right) \left[\left(1 - \varphi_{\text{CuO}}\right) \left\{ \left(1 - \varphi_{\text{Al}_{2}O_{3}}\right) + \varphi_{\text{Al}_{2}O_{3}} \frac{\rho_{\text{Al}_{2}O_{3}}}{\rho_{\text{H}_{2}O}} \right\} + \varphi_{\text{CuO}} \frac{\rho_{\text{CuO}}}{\rho_{\text{H}_{2}O}} \right] \\ &+ \varphi_{\text{TiO}_{2}} \frac{\rho_{\text{TiO}_{2}}}{\rho_{\text{H}_{2}O}} \\ &F_{2} &= \left(1 - \varphi_{\text{Al}_{2}O_{3}}\right)^{2.5} \left(1 - \varphi_{\text{CuO}}\right)^{2.5} \left(1 - \varphi_{\text{TiO}_{2}}\right)^{2.5} \\ F_{3} &= \left(1 - \varphi_{\text{TiO}_{2}}\right) \left[\left(1 - \varphi_{\text{CuO}}\right) \left\{ \left(1 - \varphi_{\text{Al}_{2}O_{3}}\right) + \varphi_{\text{Al}_{2}O_{3}} \frac{\left(\rho C_{p}\right)_{\text{Al}_{2}O_{3}}}{\left(\rho C_{p}\right)_{\text{H}_{2}O}} \right\} \right. \\ &+ \varphi_{\text{CuO}} \frac{\left(\rho C_{p}\right)_{\text{CuO}}}{\left(\rho C_{p}\right)_{\text{H}_{2}O}} \right] + \varphi_{\text{TiO}_{2}} \frac{\left(\rho C_{p}\right)_{\text{TiO}_{2}}}{\left(\rho C_{p}\right)_{\text{H}_{2}O}} \\ F_{4} &= k_{hnf} \left(\frac{k_{\text{TiO}_{2}} + 2k_{hnf} - 2\varphi_{\text{TiO}_{2}} \left(k_{hnf} - k_{\text{TiO}_{2}}\right)}{k_{\text{TiO}_{2}} + 2k_{hnf} + \varphi_{\text{TiO}_{2}} \left(k_{hnf} - k_{\text{TiO}_{2}}\right)} \right) \end{split}$$

Here,

$$\begin{split} k_{hnf} &= k_{nf} \left(\frac{k_{\text{CuO}} + 2k_{nf} - 2\varphi_{\text{CuO}} \left(k_{nf} - k_{\text{CuO}} \right)}{k_{\text{CuO}} + 2k_{nf} + \varphi_{\text{CuO}} \left(k_{nf} - k_{\text{CuO}} \right)} \right), \\ k_{nf} &= \left(\frac{k_{\text{Al}_2\text{O}_3} + 2k_{\text{H}_2\text{O}} - 2\varphi_{\text{Al}_2\text{O}_3} \left(k_{\text{H}_2\text{O}} - k_{\text{Al}_2\text{O}_3} \right)}{k_{\text{Al}_2\text{O}_3} + 2k_{\text{H}_2\text{O}} + \varphi_{\text{Al}_2\text{O}_3} \left(k_{\text{H}_2\text{O}} - k_{\text{Al}_2\text{O}_3} \right)} \right) \\ F_5 &= \sigma_{hnf} \left(\frac{\sigma_{\text{TiO}_2} + 2\sigma_{hnf} - 2\varphi_{\text{TiO}_2} \left(\sigma_{hnf} - \sigma_{\text{TiO}_2} \right)}{\sigma_{\text{TiO}_2} + 2\sigma_{hnf} + \varphi_{\text{TiO}_2} \left(\sigma_{hnf} - \sigma_{\text{TiO}_2} \right)} \right) \end{split}$$

Here,

$$\begin{split} \sigma_{hnf} &= \sigma_{nf} \left(\frac{\sigma_{\text{CuO}} + 2\sigma_{nf} - 2\varphi_{\text{CuO}} \left(\sigma_{nf} - \sigma_{\text{CuO}} \right)}{\sigma_{\text{CuO}} + 2\sigma_{nf} + \varphi_{\text{CuO}} \left(\sigma_{nf} - \sigma_{\text{CuO}} \right)} \right), \\ \sigma_{nf} &= \left(\frac{\sigma_{\text{Al}_2O_3} + 2\sigma_{\text{H}_2O} - 2\varphi_{\text{Al}_2O_3} \left(\sigma_{\text{H}_2O} - \sigma_{\text{Al}_2O_3} \right)}{\sigma_{\text{Al}_2O_2} + 2\sigma_{\text{H}_2O} + \varphi_{\text{Al}_2O_3} \left(\sigma_{\text{H}_2O} - \sigma_{\text{Al}_2O_3} \right)} \right) \end{split}$$

2.1. First-order truncation

The terms $\frac{\partial(.)}{\partial \xi}$ become vanishingly small for $\xi \ll 1$ in first-order truncation in Equations 13–16:

$$\frac{\partial P}{\partial \eta} = F_1 \frac{f'^2}{\eta + k} \tag{17}$$

$$\frac{1}{F_1} \frac{2kP}{\eta + k} = \frac{1}{F_1 F_2} \left(f''' + \frac{f''}{(\eta + k)} - \frac{f'}{(\eta + k)^2} \right) + \frac{1}{\eta + k} \times \left(kf f'' - kf'^2 + \frac{kf f'}{(\eta + k)} \right) - \frac{F_5}{F_1} \frac{k^2}{(\eta + k)^2} M^2 f' \quad (18)$$

$$\frac{F_4}{F_3} \left(\theta'' + \frac{1}{\eta + k} \theta' \right) + \Pr \frac{k}{\eta + k} f \theta' + \hat{\xi}^2 \frac{1}{F_2 F_3} \operatorname{Br} \left(f'' - \frac{f'}{\eta + k} \right)^2 + \xi^2 \operatorname{Br} \frac{F_5}{F_3} \frac{k^2}{(\eta + k)^2} M^2 f'^2 = 0$$
(19)

with

$$f'\left(\hat{\xi},0\right) = 1 + \alpha \left(f''\left(\hat{\xi},0\right) - \frac{f'}{\eta + k}\right), \quad f\left(\hat{\xi},0\right) = 0,$$

$$\theta'\left(\hat{\xi},0\right) = -\gamma_1 \left(1 - \theta\left(\hat{\xi},0\right)\right) \quad f'\left(\hat{\xi},\infty\right) \to 0,$$

$$f''\left(\hat{\xi},\infty\right) \to 0, \quad \theta\left(\hat{\xi},\infty\right) \to 0 \tag{20}$$

2.2. Second-order truncation

We have defined a new function for the second-order truncation, as shown below.

$$\frac{\partial f}{\partial \hat{\xi}} = g\left(\hat{\xi}, \eta\right), \ \frac{\partial \theta}{\partial \hat{\xi}} = h\left(\hat{\xi}, \eta\right), \ \frac{\partial P}{\partial \hat{\xi}} = L\left(\hat{\xi}, \eta\right)$$
 (21)

By utilizing Equation 21, the aforementioned Equations 13-15 may be expressed as

$$\frac{\partial P}{\partial \eta} = F_1 \frac{f'^2}{\eta + k} \tag{22}$$

$$+\frac{1}{(\eta+k)}\left(kff''-kf'^{2}+\frac{kff'}{\eta+k}\right) + \frac{1}{(\eta+k)}\left(kff''-kf'^{2}+\frac{kff'}{\eta+k}\right) - \frac{F_{5}}{F_{1}}\frac{k^{2}}{(\eta+k)^{2}}M^{2}f'$$

$$-\frac{F_{5}}{F_{1}}\frac{k^{2}}{(\eta+k)^{2}}M^{2}f'$$

$$+\frac{1}{\eta+k}\theta'\right) + \Pr\frac{k}{(\eta+k)}f\theta' + \frac{1}{\xi}\Pr\frac{k}{(\eta+k)}(\theta'g-f'h) + \frac{1}{\xi^{2}}Br\frac{1}{F_{2}F_{3}}\left(f''-\frac{f'}{\eta+k}\right)^{2} + \xi^{2}Br\frac{F_{5}}{F_{3}}\frac{k^{2}}{(\eta+k)^{2}}M^{2}f'^{2} = 0$$

$$(24)$$

 $\frac{1}{F_3} \left(\frac{2kP}{n+k} + \hat{\xi} \frac{kL}{n+k} \right) = \frac{1}{F_3 F_3} \left(f''' + \frac{f''}{n+k} - \frac{f'}{(n+k)^2} \right)$

With

$$f'(\hat{\xi}, 0) = 1 + \alpha \left(f''(\hat{\xi}, 0) - \frac{f'(\hat{\xi}, 0)}{\eta + k} \right), \quad f(\hat{\xi}, 0) + \hat{\xi}g(\hat{\xi}, 0) = 0,$$

$$\theta'(\hat{\xi}, 0) = -\gamma_1 (1 - \theta(\hat{\xi}, 0))$$

$$f'(\hat{\xi}, \infty) \to 0, \quad f''(\hat{\xi}, \infty) \to 0, \quad \theta(\hat{\xi}, \infty) \to 0$$
(25)

It is necessary to incorporate two additional equations to obtain the solution for g and h because they are two unknown functions. In this regard, we take the derivatives of Equations 22–25 with associated boundary conditions with respect to ' ζ ' and then we get

$$\frac{\partial L}{\partial \eta} = F_1 \frac{2 f' g'}{(\eta + k)} \tag{26}$$

$$\frac{1}{F_1} \left(\frac{2kL}{\eta + k} + \frac{kL}{\eta + k} \right) = \frac{1}{F_1 F_2} \left(g''' + \frac{g''}{\eta + k} - \frac{g'}{(\eta + k)^2} \right)$$

$$+ \frac{1}{\eta + k} \left(2kg f'' + kf g'' - 3k f' g' + 2 \frac{kg f'}{\eta + k} + \frac{kf g'}{\eta + k} \right)$$

$$+ \hat{\xi} \frac{k}{\eta + k} \left(g'' g - g'^2 + \frac{1}{\eta + k} g' g \right) - \frac{F_5}{F_1} \frac{k^2}{(\eta + k)^2} M^2 g'$$
(27)

$$\frac{F_4}{F_3} \left(h'' + \frac{h'}{\eta + k} \right) + \Pr \frac{k}{\eta + k} \left(2g\theta' + fh' - f'h \right) + \hat{\xi} \Pr \frac{k}{\eta + k} \left(gh' - g'h \right) \\
+ 2 \hat{\xi} Br \frac{1}{F_2 F_3} \left(f'' - \frac{f'}{\eta + k} \right)^2 + 2 \hat{\xi}^2 Br \frac{1}{F_2 F_3} \left(f'' - \frac{f'}{\eta + k} \right) \\
\times \left(g'' - \frac{g'}{\eta + k} \right) + 2 \xi Br \frac{F_5}{F_3} \frac{k^2}{(\eta + k)^2} M^2 (f')^2 \\
+ 2 \xi^2 Br \frac{F_5}{F_3} \frac{k^2}{(\eta + k)^2} M^2 f'g' = 0$$
(28)

With

$$g'(\xi',0) = \alpha \left(g''(\xi',0) - \frac{g'(\xi',0)}{\eta+k} \right), \quad g(\xi',0) = 0, \quad h'(\xi',0) = \gamma_1 h(\xi',0)$$
$$g'(\xi',\infty) \to 0, \quad g''(\xi',\infty) \to 0, \quad h(\xi',\infty) \to 0$$

(29)

Eliminating L from Equations 20 and 21, we get

$$\begin{split} &\frac{1}{F_{1}F_{2}}\left(g'''' + \frac{g'}{(\eta + k)^{3}} - \frac{g''}{(\eta + k)^{2}} + 2\frac{g'''}{\eta + k}\right) \\ &+ \frac{1}{\eta + k}\left(-kf''g' + 2kgf''' + kfg''' - 2kf'g''\right) \\ &- \frac{1}{(\eta + k)^{2}}\left(3kf'g' - kg''f - 2kf''g\right) + \frac{1}{(\eta + k)^{3}}\left(-kg'f - 2kf'g\right) \\ &- \hat{\xi}\frac{k}{\eta + k}\left(g'g'' - gg'''\right) + \hat{\xi}\frac{k}{(\eta + k)^{2}}\left(g''g + g'^{2}\right) - \hat{\xi}\frac{k}{(\eta + k)^{3}}g'g \\ &- \frac{F_{5}}{F_{1}}\frac{M^{2}k^{2}}{(\eta + k)^{2}}\left(g'' - \frac{g'}{\eta + k}\right) = 0 \end{split} \tag{30}$$

A complete system of dimensionless ordinary differential equations (ODEs) up to second-order truncation is given below.

$$\frac{1}{F_1F_2} \left(f''' + \frac{f'}{(\eta + k)^3} - \frac{f''}{(\eta + k)^2} + 2\frac{f'''}{\eta + k} \right) + \frac{1}{\eta + k} \left(kff''' - kf'f'' \right) \\
+ \frac{1}{(\eta + k)^2} \left(kf''f - 2kf'^2 \right) - \frac{1}{(\eta + k)^3} \left(kf'f \right) \\
+ \frac{1}{k} \frac{k}{(\eta + k)} \left(gf''' - f'g'' \right) + \frac{1}{k} \frac{k}{(\eta + k)^2} \left(f''g + f'g' \right) \\
- \frac{1}{k} \frac{k}{(\eta + k)^3} f'g - \frac{F_5}{F_1} \frac{M^2k^2}{(\eta + k)^2} \left(f'' - \frac{f'}{\eta + k} \right) = 0 \qquad (31)$$

$$\frac{1}{F_1F_2} \left(g''' + \frac{g'}{(\eta + k)^3} - \frac{g''}{(\eta + k)^2} + 2\frac{g'''}{\eta + k} \right) \\
+ \frac{1}{\eta + k} \left(2kgf''' - kf''g' + kfg''' - 2kf'g'' \right) \\
- \frac{1}{(\eta + k)^2} \left(3kf'g' - kg''f - 2kf''g \right) - \frac{1}{(\eta + k)^3} \left(kg'f + 2kf'g \right) \\
- \frac{1}{k} \frac{k}{\eta + k} \left(g'g'' - gg''' \right) + \frac{1}{k} \frac{k}{(\eta + k)^2} \left(g''g + g'^2 \right) \\
- \frac{1}{k} \frac{k}{\eta + k} \left(g'g'' - gg''' \right) + \frac{1}{k} \frac{k}{\eta + k} \left(g''g + g'^2 \right) \\
- \frac{1}{k} \frac{k}{F_3} \left(\theta'' + \frac{1}{\eta + k} \theta' \right) + \Pr \frac{k}{\eta + k} f\theta' + \frac{1}{k} \Pr \frac{k}{\eta + k} \left(\theta'g - f'h \right) \\
+ \frac{1}{k^2} Br \frac{1}{F_2F_3} \left(f'' - \frac{f'}{\eta + k} \right)^2 + \frac{1}{k^2} Br \frac{F_5}{F_3} \frac{k^2}{(\eta + k)^2} M^2 f'^2 = 0 \qquad (33)$$

$$\frac{F_4}{F_3} \left(h'' + \frac{h'}{\eta + k} \right) + \Pr \frac{k}{\eta + k} \left(2g\theta' + fh' - f'h \right) + \frac{1}{k} \Pr \frac{k}{\eta + k} \left(gh' - g'h \right) \\
+ 2 \frac{1}{k} Br \frac{1}{F_2F_3} \left(f'' - \frac{f'}{\eta + k} \right)^2 + 2 \frac{1}{k^2} Br \frac{F_5}{F_3} \frac{k^2}{(\eta + k)^2} M^2 f'^2 = 0 \qquad (34)$$

With

$$f'(\xi',0) = 1 + \alpha \left(f''(\xi',0) - \frac{f'}{\eta + k} \right), \quad f(\xi',0) + \xi'g(\xi,0) = 0,$$

$$f'(\xi',\infty) \to 0, \quad f''(\xi',\infty) \to 0$$

$$g'(\xi',0) = \alpha \left(g''(\xi',0) - \frac{g'}{\eta + k} \right), \quad g(\xi',0) = 0,$$

$$g'(\xi',\infty) \to 0, \quad g''(\xi',\infty) \to 0$$

$$\theta'(\xi',0) = -\gamma_1 \left(1 - \theta(\xi',0) \right), \quad \theta(\xi',\infty) \to 0,$$

$$h'(\xi',0) = \gamma_1 h(\xi',0), \quad h(\xi',\infty) \to 0$$
(35)

2.3. Field quantities of interest

The expression of fluid friction $(C_f Re_s^{\frac{1}{2}})$ and heat transfer rate $(Nu Re_s^{-\frac{1}{2}})$ is represented (Haq et al., (2024)) as

$$C_f = \frac{\tau_{rs}}{\rho_{tnf} u^2}, \quad Nu = \frac{sq_w}{k_{tnf} (T_f - T_\infty)}$$
(36)

Here, τ_{rs} and q_w are defined as

$$\tau_{rs} = \mu_{tnf} \left(\frac{\partial u}{\partial r} - \frac{u}{r+R} \right), \ q_w = -k_{tnf} \frac{\partial T}{\partial r}$$
(37)

Dimensionless forms of the above Equations 36 and 37 are

$$C_f Re_s^{\frac{1}{2}} = \frac{1}{F_2} \frac{1}{\hat{\xi}} \left(f''[0] - \frac{f'[0]}{k} \right)$$
 (38)

Nu
$$Re_s^{-\frac{1}{2}} = -F_4 \hat{\xi} \theta'[0]$$
 (39)

Here, $Re_s = \frac{a}{v}L^2$ denotes the Reynolds number.

2.4. Entropy analysis

The expression of entropy production is defined (Haq et al., 2024) as

$$\widehat{E_G} = \frac{k_{\rm tnf}}{T_{\infty}^2} \left(\frac{\partial T}{\partial r}\right)^2 + \frac{\mu_{\rm tnf}}{T_{\infty}} \left(\frac{\partial u}{\partial r} - \frac{u}{r+R}\right)^2 + \frac{\sigma_{\rm tnf} R^2 B^2 u^2}{T_{\infty} (r+R)^2}$$
(40)

In dimensionless form

$$\widehat{N}_{S} = F_{4} \beta_{1} (\theta')^{2} + \zeta^{2} \frac{\text{Ec Pr}}{F_{2}} \left(f'' - \frac{f'}{\eta + k} \right)^{2} + \zeta^{2} M^{2} F_{5} \frac{k^{2}}{(\eta + k)^{2}} \Pr \text{Ec} (f')^{2}$$
(41)

with

$$\beta_{1} = \frac{\left(T_{f} - T_{\infty}\right)}{T_{\infty}}, \ \widehat{N_{S}} = \frac{\widehat{E_{G}}\left(T_{\infty}\right)\mu_{f}}{\rho_{f}k_{f}\left(T_{f} - T_{\infty}\right)a}, \ Ec = \frac{a^{2}L^{2}}{\left(\mathbf{C_{p}}\right)_{f}\left(T_{f} - T_{\infty}\right)},$$

$$M^{2} = \frac{\sigma_{f}B^{2}}{\rho_{f}a_{f}}, \ Pr = \frac{\mu_{f}(\mathbf{C_{p}})_{f}}{k_{f}}$$

Here, \widehat{N}_S and β_1 are used to represent total entropy generation and temperature ratio parameter, respectively.

The expression for the Bejan number is as follows:

$$Be = \left\{ \frac{\beta_1 F_4(\theta')^2}{\beta_1 F_4(\theta')^2 + \xi^2 \frac{EC Pr}{F_2} \left(f'' - \frac{f'}{\eta + k} \right)^2} + \xi^2 F_5 \frac{k^2}{(\eta + k)^2} M^2 EC Pr \left(f' \right)^2} \right\}$$
(42)

3. Numerical Solution

Numerical approaches necessitate reduced calculation time and yield approximately close analytical solutions. This study employs the MATLAB built-in numerical approach bvp4c to get the solution of coupled non-linear ODEs (31)–(34) with the associated boundary condition, utilizing a finite-difference scheme with Lobatto IIIA. In this problem, the relative error tolerance is established 1×10^{-6} using the bvpset function to enhance accuracy. We take an initial guess of 0.01 for each dependent variable at the mesh points using the bvpinit function. Figure 3 shows the complete methodology procedure given below.

4. Results and Discussion

In this section, the numerical results of fluid velocity, temperature, entropy, and Bejan number are obtained for the various physical parameters utilizing Bvp4c. The flowchart associated with

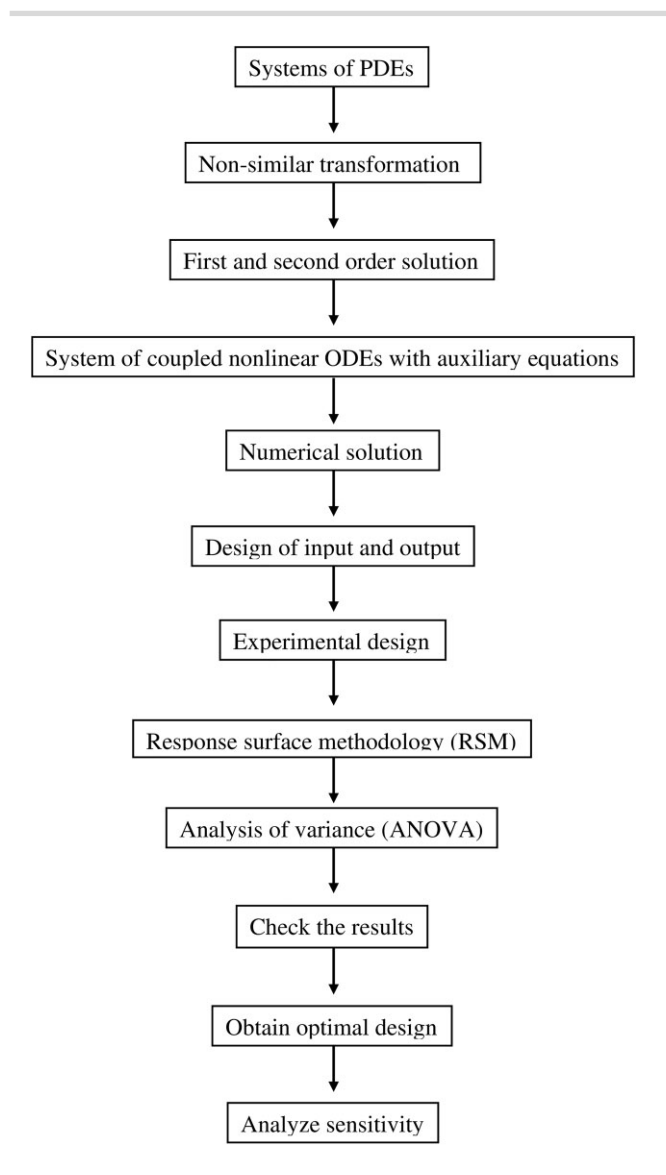


Figure 2: Flow chart of the problem.

the problem is depicted in Figure 2. The values of physical parameters are taken from the relevant literature to ensure a stable and physically significant solution. In this problem, small values for the parameter are considered due to laminar boundary flow. A small amount of nanoparticles (ϕ < 0.01) in the base fluid can significantly improve the thermal conductivity. This is due to the fact that nanometre-sized nanoparticles behave like fluid molecules, which allow for an increase in thermal conductivity. Therefore, we choose a smaller volume fraction of nanoparticles in the base fluid. The Biot number values are considered small because they signify that heat transfer is primarily controlled by convection at the surface rather than internal conduction within the solid. For industrial applications, moderate Prandtl numbers (Pr = 1-100) apply to heat exchangers, turbine blade cooling, and polymer stretching processes. Small Hartmann numbers (M < 20) are useful in MHD-based cooling of aerospace components, while controlled nanoparticle volume fractions ($\phi =$ 0.01-0.05) increase thermal performance in advanced engineering systems.

4.1. Velocity profile

Figures 4–6 show the velocity profile for the variation of Hartmann number, volume fraction, and slip parameter. Figure 4 displays the trend of fluid velocity as a function of Hartmann number. It is observed that as the Hartmann number increases, the magnetic damping effect causes the fluid velocity in boundary layer flow to decrease. A greater Hartmann number indicates a stronger magnetic field, which causes a larger Lorentz force opposing the fluid motion. This force works like a magnetic drag, opposing the flow and slowing the velocity. In Figure 5, the behaviour of velocity is depicted for ternary nanofluids with increasing amounts of volume fraction. The solid volume fraction of nanoparticles enhances the fluid velocity because more particles are added to the fluid and decrease the viscosity and density, improving mixing within the fluid, so it increases the fluid velocity. Figure 6 depicts the slip parameter's impact on fluid velocity. It is observed that the slip parameter decreases the velocity due to less friction occurring between the fluid and the surface as a result of the increased slip parameter, which causes the fluid velocity to decrease.

4.2. Temperature profile

Figure 7 displays fluid temperature increase for rising values of a Hartmann number due to a higher magnetic field causing more resistive heating in an electrically conducting fluid; more electrical energy is converted to heat and thus raises the fluid's temperature when the Hartmann number rises. Figure 8 displays the temperature profile's behaviour as a function of increasing volume fraction values for ternary nanofluids. The fluid temperature increases as the volume fraction of nanoparticles increases because the nanoparticles improve thermal conductivity, which increases heat transfer and boosts fluid temperatures. Higher particle concentrations may also generate more frictional heat and improve the fluid's thermal resistance, both of which contribute to temperature increases. Figure 9 depicts the influence of rising values of the Eckert number on the temperature profile. When the Eckert number rises, it indicates that kinetic energy in a fluid flow is becoming more significant than thermal energy. This occurs because, via processes like viscous dissipation, more kinetic energy is available to be transformed into thermal energy as the flow velocity rises. Consequently, a larger Eckert number causes the fluid's temperature to rise as a consequence of this increased kinetic energy conversion to heat, raising the fluid's temperature overall. Figure 10 illustrates the influence of the Biot number on the temperature distribution. When the Biot number rises, it signifies that the solid's internal thermal resistance is higher than the heat transfer occurring at its surface. The fluid temperature at the contact rises as a consequence of this inefficient heat transfer from the solid to the fluid. As a result, as the Biot number rises, so does the fluid temperature.

4.3. Entropy and Bejan number

Figure 11 illustrates the influence of the Hartmann number on the production of entropy. These effects intensify the inhibition of fluid motion and raise viscous strains, which raises the system's entropy production and energy dissipation. Figure 12 depicts the influence of volume fraction on the entropy production. It has been shown that ternary nanofluids exhibit enhanced thermal conductivity and viscosity as the volume percentage of nanoparticles in the fluid increases. Higher viscous dissipation and increased flow resistance as a result boost the conversion of energy into thermal energy. As a result of the fluid flow's

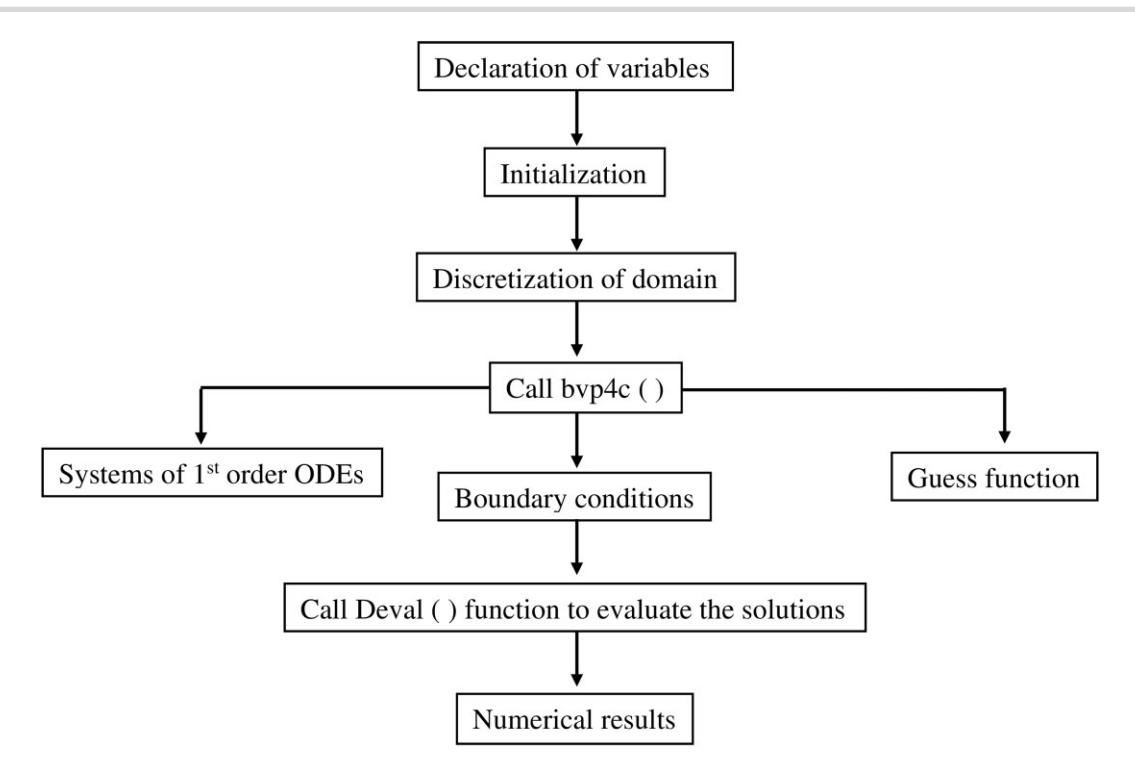


Figure 3: Flow chart of methodology.

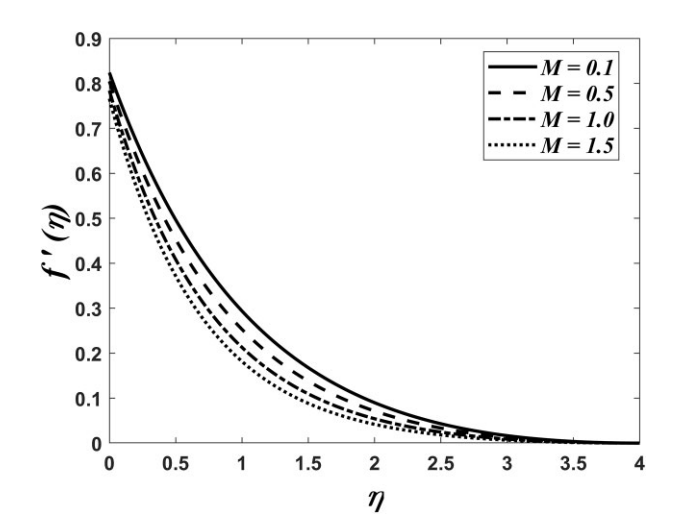


Figure 4: Effect of Hartmann on velocity field.

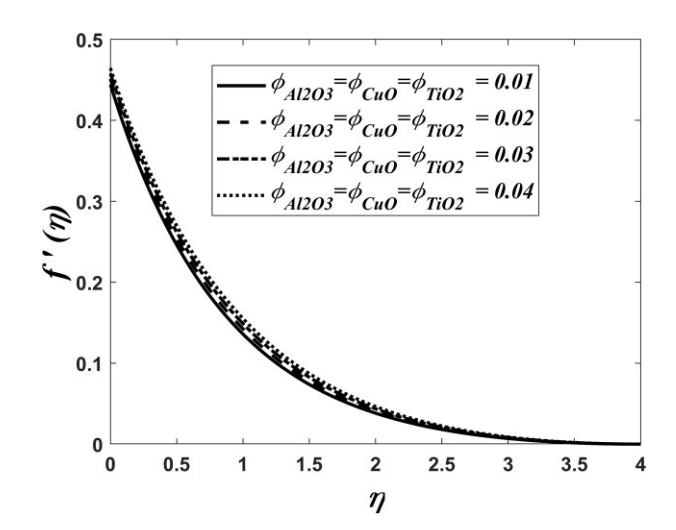


Figure 5: Effect of volume fraction coefficients on velocity field.

enhanced irreversibility, entropy production increases. The impact of the Eckert number of entropy generation is shown in Figure 13. It is observed that the rising values of the Eckert number cause an enhancement of the entropy production because it leads to a higher conversion of kinetic energy into heat; as a result, greater entropy production. Figure 14 shows the influence of Hartmann number on Bejan number. An increasing value of the Hartmann number leads to a decrease in the Bejan number near the boundary $\eta = 0.5$, which it starts increasing because magnetic fields reduce fluid velocity and strengthen thermal boundary layers as Hartmann numbers increase. As a result, heat transmission becomes relatively more dominant than fluid movement, raising the Bejan number. Figure 15 depicts the behaviour of the

Bejan number within the context of increasing values of volume fraction of nanoparticles. It is observed that the Bejan number is reduced due to the greater values of volume fraction because it indicates a lower ratio of heat transfer to overall entropy production, which lowers the Bejan number. Figure 16 depicts the influence of the Eckert number on the Bejan number. The total amount of entropy generated is increased by the Eckert number because the frictional effect is more prominent in the fluid. Table 3 provides the numerical values of skin friction and heat transfer rate for the different physical parameters along with a comparison of BVP4C and the shooting method. It indicates that the rising values of Hartmann number, volume fraction, and Eckert number decrease the fraction at the surface while the slip parameter

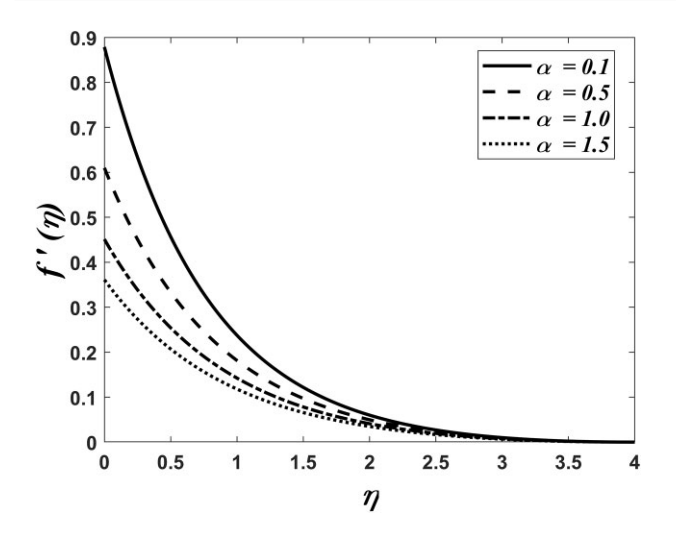


Figure 6: Effect of slip parameter on velocity field.

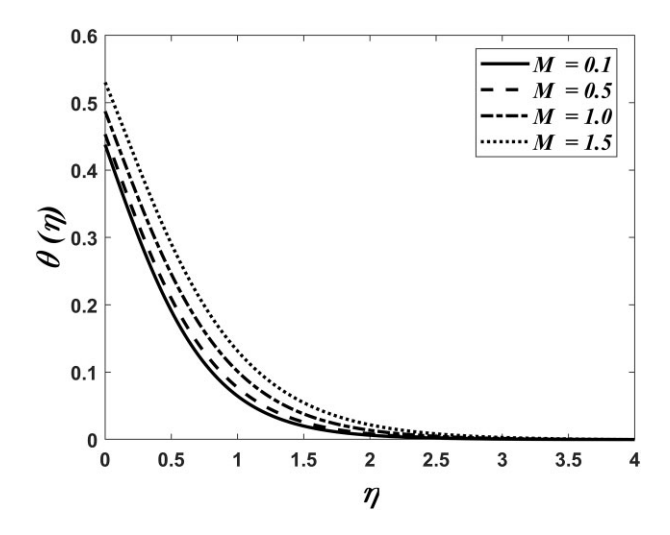


Figure 7: Effect of Hartmann number on temperature profile.

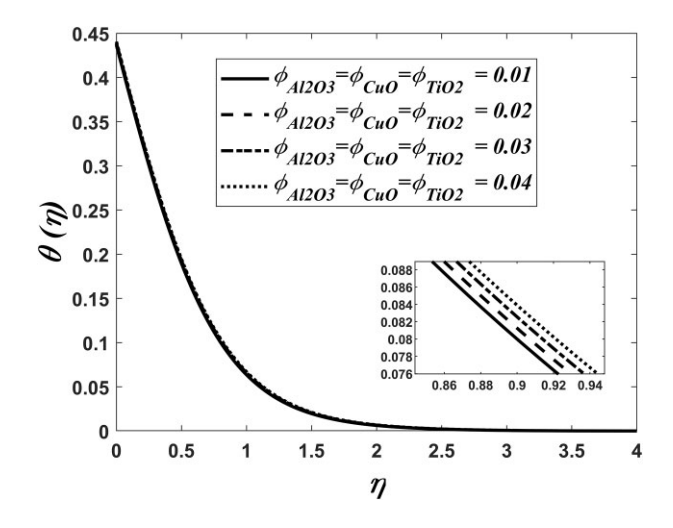


Figure 8: Effect of volume fraction coefficients on temperature profile.

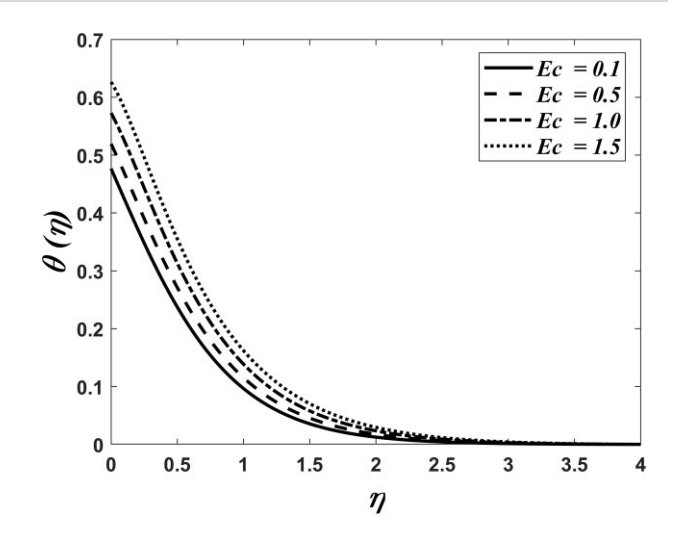


Figure 9: Effect of Eckert number on temperature profile.

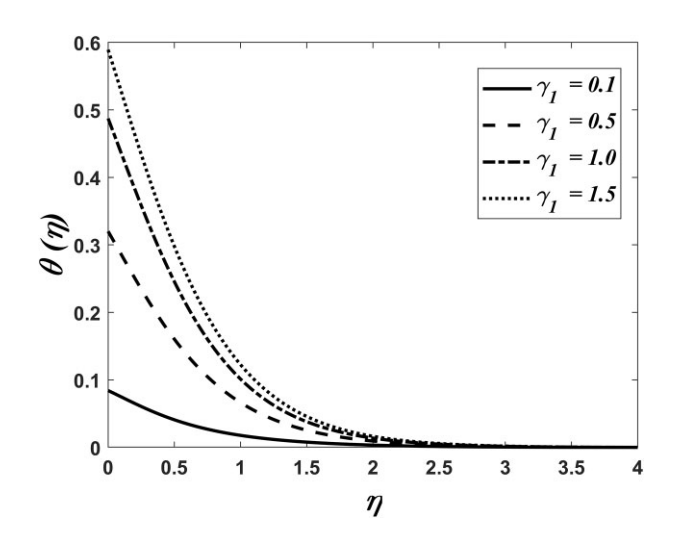


Figure 10: Effect of Biot number on temperature profile.

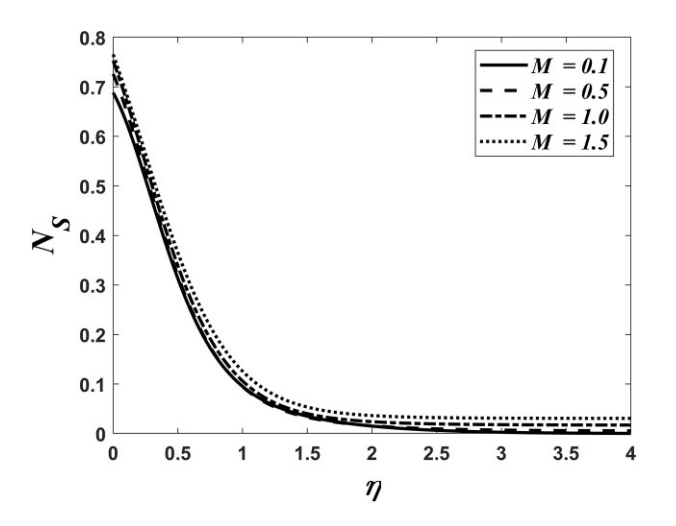


Figure 11: Effect of Hartmann number on entropy generation.

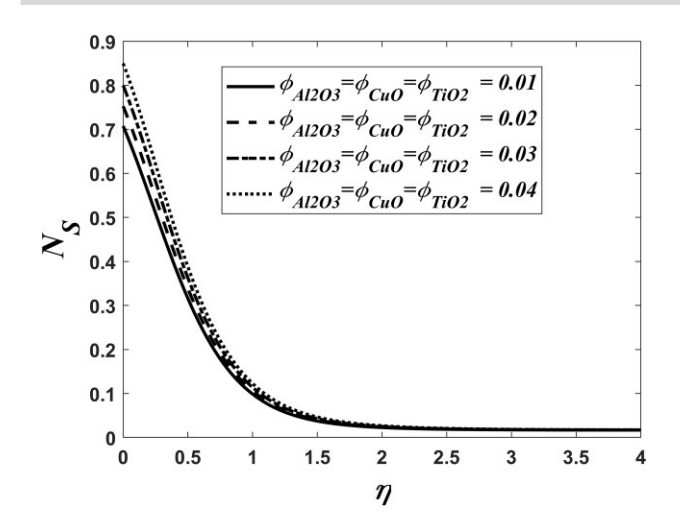


Figure 12: Effect of volume fraction coefficients on entropy generation.

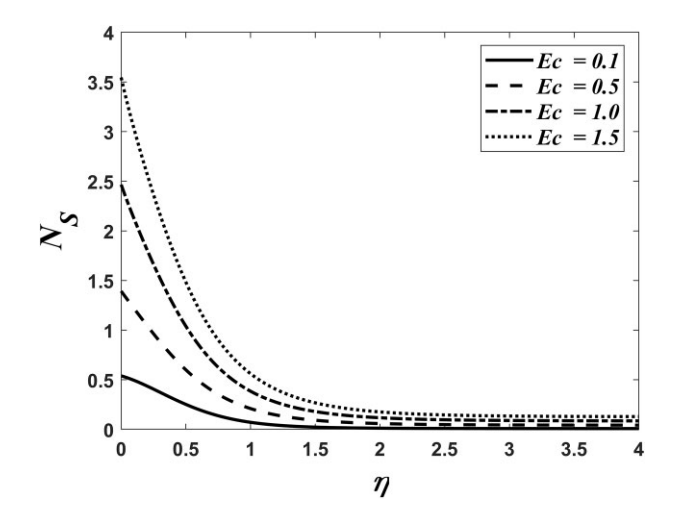


Figure 13: Effect of Eckert number on entropy generation.

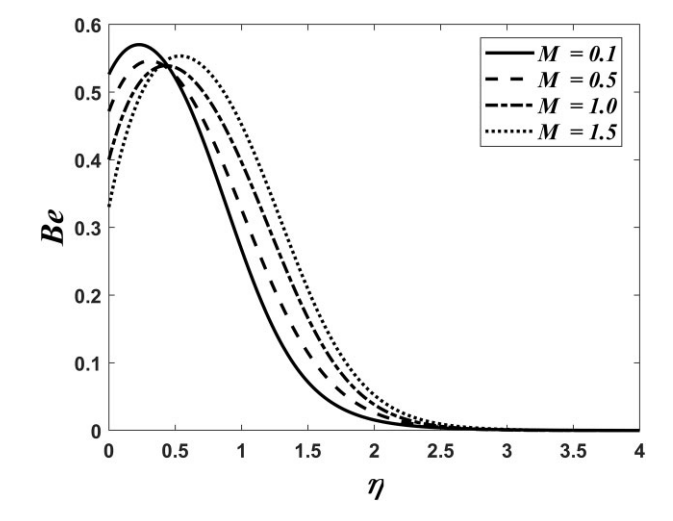


Figure 14: Effect of Hartmann number on Bejan number.

increases it. On the other hand, heat transfer rate is increased for the Biot number and volume fraction, but the Hartmann number, Eckert number, and slip parameter decrease it. Table 4 shows the relative percentage error between the first- and second-

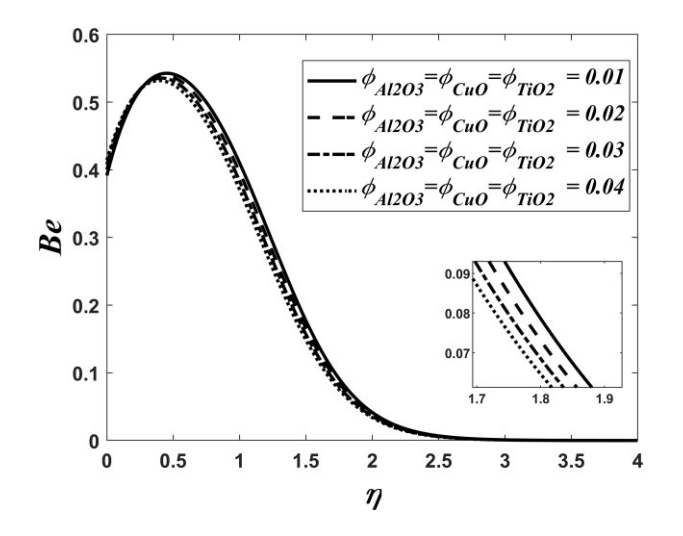


Figure 15: Effect of volume fraction coefficients on Bejan number.

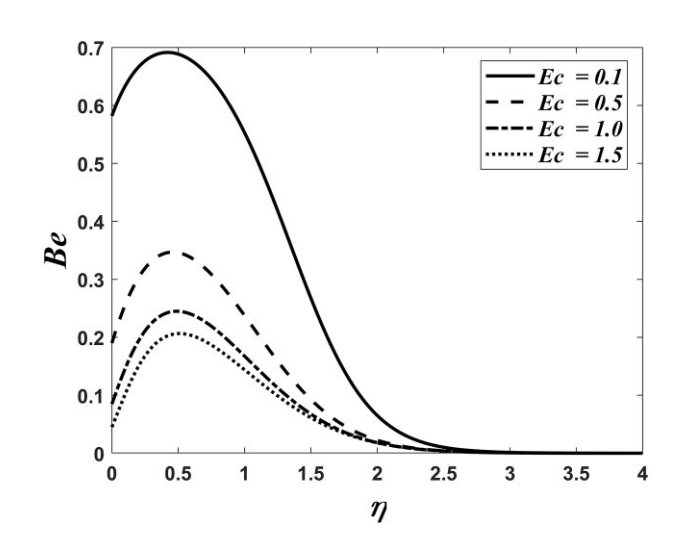


Figure 16: Effect of volume Eckert number on Bejan number.

order truncation for rising values of Hartmann number. Relative error is increasing among truncation for increasing Hartmann number.

5. Response Surface Methodology

RSM is a method for optimizing responses, where there are two or more input parameters. The independent variables, or factors, are referred to as input variables in RSM, whereas the dependent variables are called responses. The correlations between drag force $(C_f Re_s^{\frac{1}{2}})$ and heat transfer rate $(Nu Re_s^{-\frac{1}{2}})$ are treated as the output responses; the Hartmann number (M), slip parameter (α), and volume fraction coefficient (φ) are input parameters for response drag force, while the volume fraction coefficient (φ), Biot number (γ_1) , and Hartmann number (M) are treated as input parameters for heat transfer rate. These input parameters are evaluated at three coded levels: low (-1), medium (0), and high (+1) to examine their combined effect on the output responses. These parameters' linear, quadratic, and interaction impacts may all be captured by expanding the quadratic model used for this study, which is writ-

Table 3: Computational values of skin friction and local Nusselt number when $\zeta = 1$.

М	α	φ	Ec	γ	C _f Re _s ^{0.5} Bvp4c	$C_f Re_s^{0.5}$ Shooting method	Nu Re _s ^{-0.5} Bvp4c	Nu Re _s ^{-0.5} Shooting method
1	0.2	0.01	0.2	0.8	-1.164446	-1.164445	0.535555	0.535554
2					-1.346018	-1.346017	0.376820	0.376819
3					-1.490716	-1.490715	0.143654	0.143653
0.8	0.4				-0.905817	-0.905816	0.537661	0.537660
	0.7				-0.708555	-0.708554	0.516222	0.516221
	1.0				-0.584581	-0.584580	0.498349	0.498348
	0.2	0.02			-1.192933	-1.192932	0.595642	0.595641
		0.03			-1.268882	-1.268881	0.638189	0.638188
		0.04			-1.350112	-1.350110	0.682844	0.682843
		0.01	0.4		-1.121858	-1.121857	0.540601	0.540600
			0.6		-1.121859	-1.121858	0.525432	0.525431
			0.8		-1.121860	-1.121859	0.510689	0.510688
			0.2	1.2	-1.121858	-1.121857	0.699216	0.699215
				1.6	-1.121858	-1.121857	0.802060	0.802059
				2.0	-1.121858	-1.121857	0.878647	0.878646

Table 4: Relative error for the first- and second-order truncation when $\zeta = 0.1$, Ec = 0.2, $\alpha = 0.2$, $\gamma = 0.8$, and k = 15.

	Local Nusselt number							
M	1 st truncation	Relative error	2 nd truncation					
0.2	0.0577153212	0.2331%	0.0578501846					
0.9	0.0566140285	0.3442%	0.0568095726					
1.6	0.0555499191	0.4337%	0.0557918950					
2.3	0.0545147324	0.5100%	0.0547942282					
3.0	0.0535023545	0.5778%	0.0538133249					

Table 5: Ranges of input parameters for $(C_f Re_s^{\frac{1}{2}})$.

				Levels	
Symbol	Factors	Ranges	Lower (-1)	Central (0)	Higher (+1)
A1	M	$0.1 \le M \le 1.5$	0.1	0.8	1.5
B2	α	$0.1 \le \alpha \le 1.5$	0.1	0.8	1.5
C1	$\varphi_{\text{Al}_2\text{O}_3} =$	$0.01 \le \varphi \le 0.04$	0.01	0.025	0.04
	$\varphi_{\mathrm{CuO}} =$				
	$\varphi_{\mathrm{TiO}_2} = \varphi$				

Table 6: Ranges of input parameters for (Nu Re_s^{$-\frac{1}{2}$}).

			Levels		
Symbol	Factors	Ranges	Lower (-1)	Central (0)	Higher (+1)
A1	М	0.1 ≤ M ≤ 1.5	0.1	0.8	1.5
B1	γ_1	$0.1 \le \gamma_1 \le 1.5$	0.1	0.8	1.5
C1	$\varphi_{\text{Al}_2\text{O}_3} =$	$0.01 \le \varphi \le 0.04$	0.01	0.025	0.04
	$\varphi_{\mathrm{CuO}} =$				
	$\varphi_{\mathrm{TiO}_2} = \varphi$				

$$C_{f}Re_{s}^{\frac{1}{2}} = \alpha_{0} + \alpha_{1}M + \alpha_{2}\alpha + \alpha_{3}\varphi + \alpha_{11}M\alpha + \alpha_{12}M\varphi + \alpha_{13}\alpha\varphi$$

$$+ \alpha_{21}M^{2} + \alpha_{22}\alpha^{2} + \alpha_{23}\varphi^{2}$$

$$(43)$$

Table 7: Real and coded values of the $(C_f Re_s^{\frac{1}{2}})$.

Run	(Coded value	es	Para	meters	values	Response
	Low	Middle	High	М	α	φ	$C_f Re_s^{\frac{1}{2}}$
1	-1	-1	-1	0.1	0.1	0.010	-1.07014
2	1	-1	-1	1.5	0.1	0.010	-1.45416
3	-1	1	-1	0.1	1.5	0.010	-0.40994
4	1	1	-1	1.5	1.5	0.010	-0.48422
5	-1	-1	1	0.1	0.1	0.040	-1.34726
6	1	-1	1	1.5	0.1	0.040	-1.70040
7	-1	1	1	0.1	1.5	0.040	-0.51460
8	1	1	1	1.5	1.5	0.040	-0.58760
9	-1	0	0	0.1	0.8	0.025	-0.65297
10	1	0	0	1.5	0.8	0.025	-0.78582
11	0	-1	0	0.8	0.1	0.025	-1.40200
12	0	1	0	0.8	1.5	0.025	-0.50258
13	0	0	-1	0.8	0.8	0.010	-0.66147
14	0	0	1	0.8	0.8	0.040	-0.80447
15	0	0	0	0.8	0.8	0.025	-0.72883
16	0	0	0	0.8	0.8	0.025	-0.72883
17	0	0	0	0.8	0.8	0.025	-0.72883
18	0	0	0	0.8	0.8	0.025	-0.72883
19	0	0	0	0.8	0.8	0.025	-0.72883
20	0	0	0	0.8	0.8	0.025	-0.72883

Nu
$$\operatorname{Re}_{s}^{-\frac{1}{2}} = \beta_{0} + \beta_{1}M + \beta_{2}\gamma_{1} + \beta_{3}\varphi + \beta_{11}M\gamma_{1} + \beta_{12}M\varphi + \beta_{13}\gamma_{1}\varphi + \beta_{21}M^{2} + \beta_{22}\gamma_{1}^{2} + \beta_{23}\varphi^{2}$$
 (44)

where the drag force and heat transfer rate are represented by $C_f Re_s^{\frac{1}{2}}$ and Nu $Re_s^{-\frac{1}{2}}$. Here,

the symbol α_0 and β_0 are used to represent the intercept ef-

the coefficients of linear effects are represented by α_i and β_i where i = 1, 2, 3; and

the quadratic and interaction effects of the input components are represented by α_{ij} , β_{ij} where i = j = 1, 2, 3.

The quadratic model is imposed using the inbuilt CCD via a face-centred approach, which enables the estimate of unknown coefficients using RSM. RSM used 20 experimental runs and 19

Table 8: Real and coded values of the (Nu Re_s^{$-\frac{1}{2}$}).

	(Coded value	es	Para	meters	values	Response
Run	Low	Middle	High	M	γ 1	φ	Nu Res - 1
1	-1	-1	-1	0.1	0.1	0.010	0.1006337
2	1	-1	-1	1.5	0.1	0.010	0.0925810
3	-1	1	-1	0.1	1.5	0.010	0.7399574
4	1	1	-1	1.5	1.5	0.010	0.5878059
5	-1	-1	1	0.1	0.1	0.040	0.1227242
6	1	-1	1	1.5	0.1	0.040	0.1150665
7	-1	1	1	0.1	1.5	0.040	0.8933948
8	1	1	1	1.5	1.5	0.040	0.7517130
9	-1	0	0	0.1	0.8	0.025	0.5845649
10	1	0	0	1.5	0.8	0.025	0.4997961
11	0	-1	0	0.8	0.1	0.025	0.1101370
12	0	1	0	0.8	1.5	0.025	0.7562305
13	0	0	-1	0.8	0.8	0.010	0.4983494
14	0	0	1	0.8	0.8	0.040	0.6146586
15	0	0	0	0.8	0.8	0.025	0.5547521
16	0	0	0	0.8	0.8	0.025	0.5547521
17	0	0	0	0.8	0.8	0.025	0.5547521
18	0	0	0	0.8	0.8	0.025	0.5547521
19	0	0	0	0.8	0.8	0.025	0.5547521
20	0	0	0	0.8	0.8	0.025	0.5547521

Table 9: Regression coefficient of $(C_f Re_s^{\frac{1}{2}})$.

Term	Coef	SE coef	T-value	P-value	VIF	Significance
Constant	- 0.72897	0.00677	- 107.74	0.000		Yes
M	-0.10173	0.00622	- 16.35	0.000	1.00	Yes
α	0.44750	0.00622	71.90	0.000	1.00	Yes
φ	-0.08744	0.00622	-14.05	0.000	1.00	Yes
M*M	0.0098	0.0119	0.82	0.429	1.82	No
α*α	-0.2231	0.0119	-18.80	0.000	1.82	Yes
$\varphi*\varphi$	-0.0038	0.0119	-0.32	0.756	1.82	No
M∗α	0.07373	0.00696	10.60	0.000	1.00	Yes
$M*\varphi$	0.00402	0.00696	0.58	0.576	1.00	No
$\alpha*\varphi$	0.03941	0.00696	5.66	0.000	1.00	Yes

Table 10: ANOVA results of $(C_f Re_s^{\frac{1}{2}})$.

Source	DF	Adj SS	Adj MS	F-value	P-value	Significance
Model	9	2.47978	0.27553	711.37	0.000	Yes
Linear	3	2.18253	0.72751	1878.29	0.000	Yes
Square	3	0.24121	0.08040	207.58	0.000	Yes
2-way	3	0.05605	0.01868	48.24	0.000	Yes
interaction						
Error	10	0.00387	0.00039			
Lack of fit	5	0.00387	0.00077			
Pure error	5	0.00000	0.00000			
Total	19	2.48366				
		$R^2 = 99$.84%, R ² (A	Adj) = 99.7	0%	

degrees of freedom to determine how the input parameter affected the output in this study. This model provides the optimal value of the Biot number, slip parameter, Hartmann number, and volume fraction of ternary nanofluids that maximize or minimize the skin friction $(C_f Re_s^{\frac{1}{2}})$ and the local Nusselt number $(Nu Re_s^{-\frac{1}{2}})$.

Table 11: Regression coefficient of (Nu Re_s^{$-\frac{1}{2}$}).

Term	Coef	SE coef	T-value	P-value	VIF	Significance
Constant	0.55430	0.00204	272.24	0.000		Yes
M	-0.03943	0.00187	-21.05	0.000	1.00	Yes
γ_1	0.31880	0.00187	170.22	0.000	1.00	Yes
φ	0.04782	0.00187	25.53	0.000	1.00	Yes
M*M	-0.01144	0.00357	-3.20	0.009	1.82	Yes
$\gamma_1 * \gamma_1$	-0.12043	0.00357	-33.72	0.000	1.82	Yes
$\varphi*\varphi$	0.00289	0.00357	0.81	0.438	1.82	No
$M*\gamma_1$	-0.03477	0.00209	-16.60	0.000	1.00	Yes
$M*\varphi$	0.00136	0.00209	0.65	0.531	1.00	No
$\gamma_1*\varphi$	0.03410	0.00209	16.28	0.000	1.00	Yes

Table 12: ANOVA results of (**Nu** $Re_s^{-\frac{1}{2}}$).

Source	DF	Adj SS	Adj MS	F-value	P-value	Significance
Model	9	1.15291	0.12810	3652.00	0.000	Yes
Linear	3	1.05473	0.35158	10022.98	0.000	Yes
Square	3	0.07920	0.02640	752.60	0.000	Yes
2-way	3	0.01898	0.00633	180.40	0.000	Yes
interaction						
Error	10	0.00035	0.00004			
Lack of fit	5	0.00035	0.00007			
Pure error	5	0.00000	0.00000			
Total	19	1.15326				
		$R^2 = 99$	9.97%, R ² (.	Adj) = 99.9	4%	

Tables 5 and 6 show the ranges of different levels of values for skin friction and local Nusselt number. Tables 7 and 8 show the real and coded values of the experimental design for skin friction and local Nusselt number.

6. Analysis of Variance

When evaluating regression models and doing other statistical tests (F-values, p-values, etc.), ANOVA is an essential statistical technique. Tables 9 and 11 show all the tests and their simulations that are performed for the skin friction $(C_f Re_s^{\frac{1}{2}})$ and the local Nusselt number (Nu $Re_s^{-\frac{1}{2}}$). These tests are performed at a 95% confidence level, which corresponds to a 5% significance level. According to the preliminary data, F-values over one and p-values less than 0.05 are required for higher model accuracy. A final expression for the suggested model of the skin friction and Nusselt number is given in Equations 47 and 48, which are modified by removing interaction terms based on the results in Tables 10 and 12 (from the ANOVA) and the ranges of the components with their associated p-values. The calculated R^2 value for skin friction is 99.84%, and the Nusselt number is 99.97%, indicating that the proposed models fit the data quite well. Similarly, the Nusselt number and skin friction both have adjusted values of 99.94% and 99.70%, respectively. Figures 17A-D and 18A-D show that the skin friction and the local Nusselt number models match the RSM analysis quite well, with adj R2 values of 99.70% and 99.94% and R² values of 99.84% and 99.97%, respectively. The residuals plot for both models' normal probability plots shows that they are almost straight lines, indicating that they are normally distributed, which validates the model's assumptions. The residual histograms show a bell-shaped, balanced curve around zero, indicating a regularly distributed set of errors. The

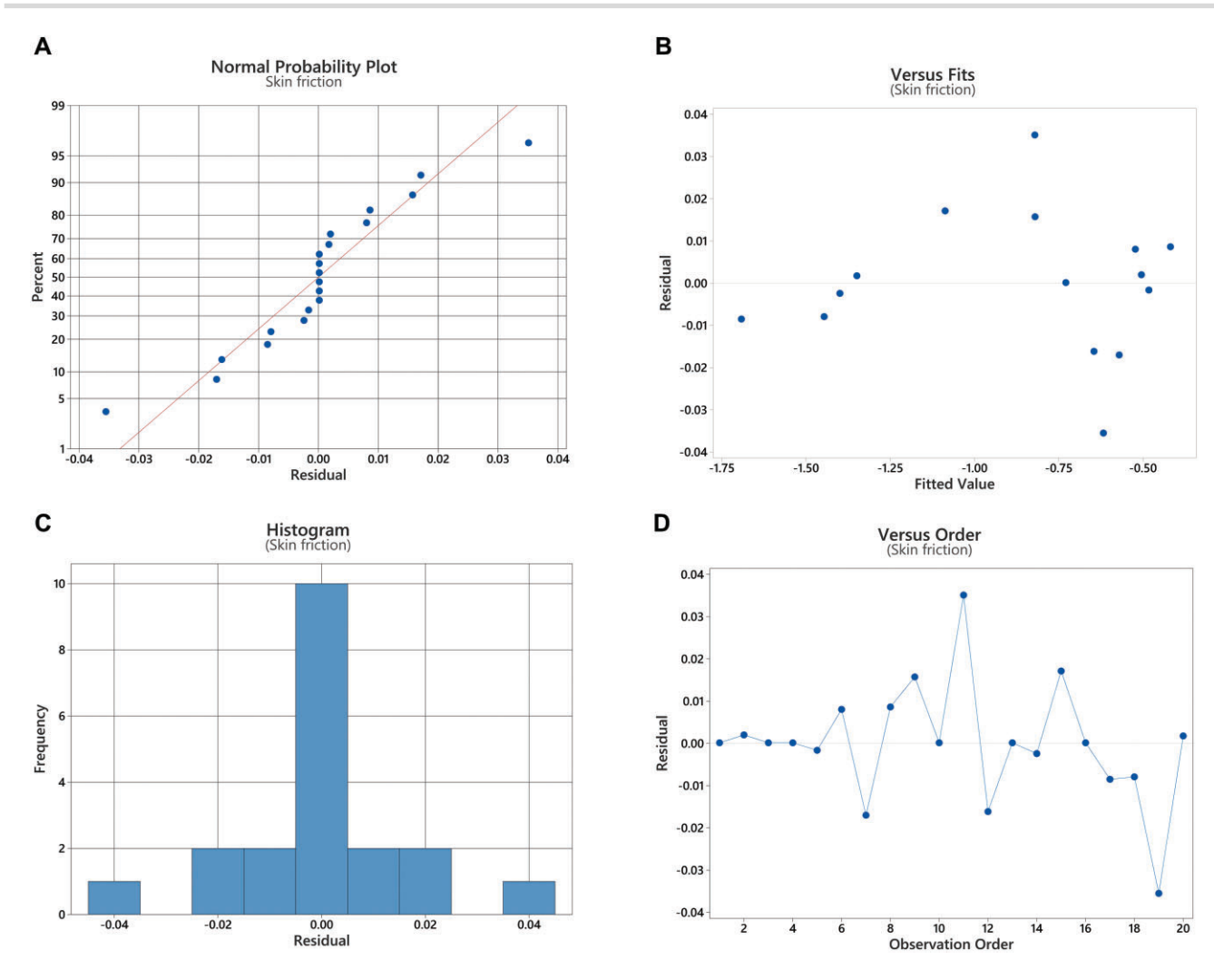


Figure 17: Residual plot for skin friction. (A) Normal probability. (B) Residuals versus fits. (C) Histogram. (D) Residuals versus order.

plots of residuals against fit show a disorganized distribution of points around the zero line, indicating the absence of any patterns and the consistency of the model mistakes. Ultimately, the absence of discernible trends over time in the residuals versus order graphs suggests that the residuals are independent and the models are trustworthy for forecasting skin friction and the Nusselt

$$\begin{split} C_f Re_s^{\frac{1}{2}} &= -0.72897 - 0.10173M + 0.44750\alpha - 0.08744\varphi + 0.07373M\alpha \\ &+ 0.00402M\varphi + 0.03941\alpha\varphi + 0.0098M^2 - 0.2231\alpha^2 \\ &- 0.0038\varphi^2 \end{split} \tag{45} \\ Nu \ Re_s^{-\frac{1}{2}} &= 0.55430 - 0.03943M + 0.31880\gamma_1 + 0.04782\varphi \\ &- 0.03477M\gamma_1 + 0.00136M\varphi + 0.03410\gamma_1\varphi - 0.01144M^2 \\ &- 0.12043\gamma_1^2 + 0.00289\varphi^2 \end{aligned} \tag{46}$$

By removing the insignificant variables from the above Equations 45 and 46, we obtain

$$\begin{split} C_f Re_s^{\frac{1}{2}} &= -0.72897 - 0.10173M + 0.44750\alpha - 0.08744\varphi \\ &\quad + 0.07373M\alpha + 0.03941\alpha\varphi - 0.2231\alpha^2 \end{split} \tag{47}$$

Nu Results =
$$0.55430 - 0.03943M + 0.31880\gamma_1 + 0.04782\varphi$$

- $0.03477M\gamma_1 + 0.03410\gamma_1\varphi - 0.01144M^2 - 0.12043\gamma_1^2$ (48)

Figures 19A-C and 20A-C show the surface contour plots for drag force $(C_f Re_s^{\frac{1}{2}})$ and heat transfer rate $(Nu Re_s^{-\frac{1}{2}})$, respectively. Figure 19A illustrates the behaviour of skin friction for all the levels of Hartmann number and the slip parameter, while the volume fraction coefficient $(C_f Re_s^{\frac{1}{2}})$ is considered the middle value (0). The skin friction is maximum at the low value (-1) of the Hartmann number and high value (+1) at the slip parameter. Figure 19B shows the impact of Hartmann number and volume fraction on skin friction coefficient for the middle value (0) of the slip parameter. It is observed that the skin friction $(C_f Re_s^{\frac{1}{2}})$ is maximum at the lower values (-1) of both M and φ . Figure 19C displays the effect of volume fraction and slip parameter with the middle (0) of the Hartmann number on the skin friction ($C_f Re_2^{\frac{1}{2}}$). It is noticed that the skin friction is maximum at the higher values (+1) of volume fraction and slip parameter. Figure 20A shows the influence of Hartmann and Biot numbers on the Nusselt number, with the volume fraction coefficient taken as the middle value

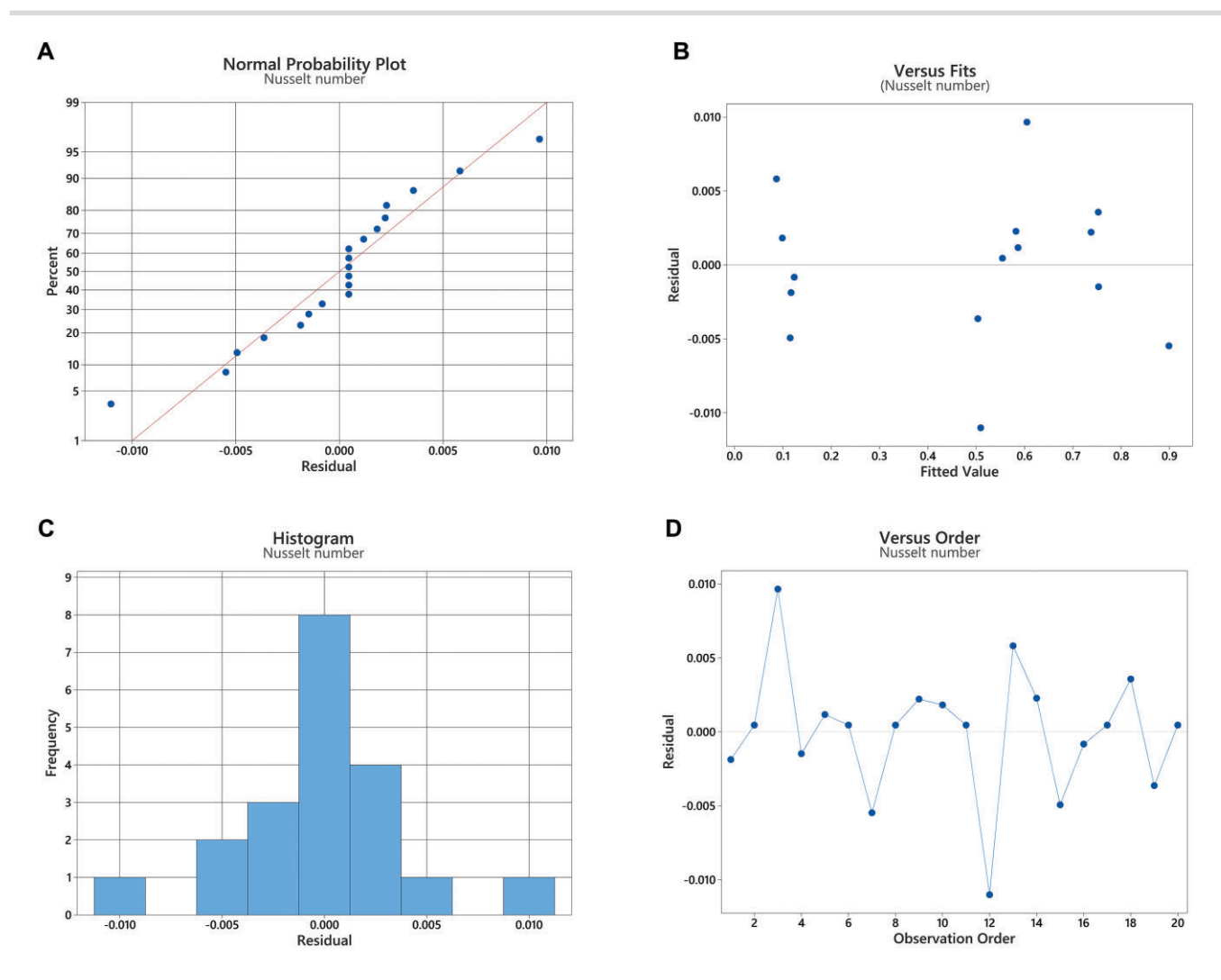


Figure 18: Residual plot for Nusselt number. (A) Normal probability. (B) Residuals versus fits. (C) Histogram. (D) Residuals versus order.

(0). The Nusselt number's ($Nu~Re_s^{-\frac{1}{2}}$) maximum occurs at the low value (-1) of the Hartmann number and the high value (+1) at the Biot number. Figure 20B shows the impact of Hartmann number and volume fraction on Nusselt number for the middle value (0) of the Biot number. It is observed that the Nusselt number ($Nu~Re_s^{-\frac{1}{2}}$) is maximum at the lower values (-1) of the Hartmann number, and volume fraction is maximum at the higher value (+1). Figure 20C illustrates the impact of volume fraction and the Biot number on skin friction, specifically when the Hartmann number is at its midpoint (0). It is noticed that the heat transfer rate ($Nu~Re_s^{-\frac{1}{2}}$) reaches its highest value in the upper range (+1) of volume fraction and Biot number.

7. Sensitivity Analysis

To find out which input parameter has the most impact on the output responses, sensitivity analysis is used. In this problem, friction at the wall $(C_fRe_s^{\frac{1}{2}})$ and heat transfer rate $(Nu\,Re_s^{-\frac{1}{2}})$ are affected by input factors, including the M, α , γ_1 , and φ . In order to regulate the precision and efficiency of fluid flow problems, this study is crucial for figuring out which input parameter is most significant and more impactful. The mathematical representation of sensitivity analysis is the partial derivatives of the dependent

variable (output) with respect to the independent variables (input). On the basis of the independent variables, the partial derivatives are computed in the following manner:

$$\frac{\partial C_f}{\partial M} = -0.10173 + 0.07373\alpha \tag{49}$$

$$\frac{\partial C_f}{\partial \alpha} = 0.44750 + 0.07373M + 0.03941\varphi - 2(0.2231)\alpha$$
 (50)

$$\frac{\partial C_f}{\partial x_0} = -0.08744 + 0.03941 \tag{51}$$

$$\frac{\partial Nu}{\partial M} = -0.03943 - 0.03477\gamma_1 - (2) 0.01144M \tag{52}$$

$$\frac{\partial Nu}{\partial \nu_1} = 0.31880 - 0.03477M + 0.03410\varphi - (2) 0.12043\gamma_1$$
 (53)

$$\frac{\partial Nu}{\partial \omega} = 0.04782 + 0.03410\gamma_1 \tag{54}$$

Figures 21 and 22 illustrate the sensitivity of the drag force and heat transfer rate with respect to each input parameter. In these figures, a positive bar indicates that the response increases when the input parameter increases, while a negative bar indicates that the response decreases when the input parameter increases. Each bar's height represents the magnitude of sensitivity: the taller the bar, the more sensitive the response is to that particular parameter. Thus, the parameter that was found to be

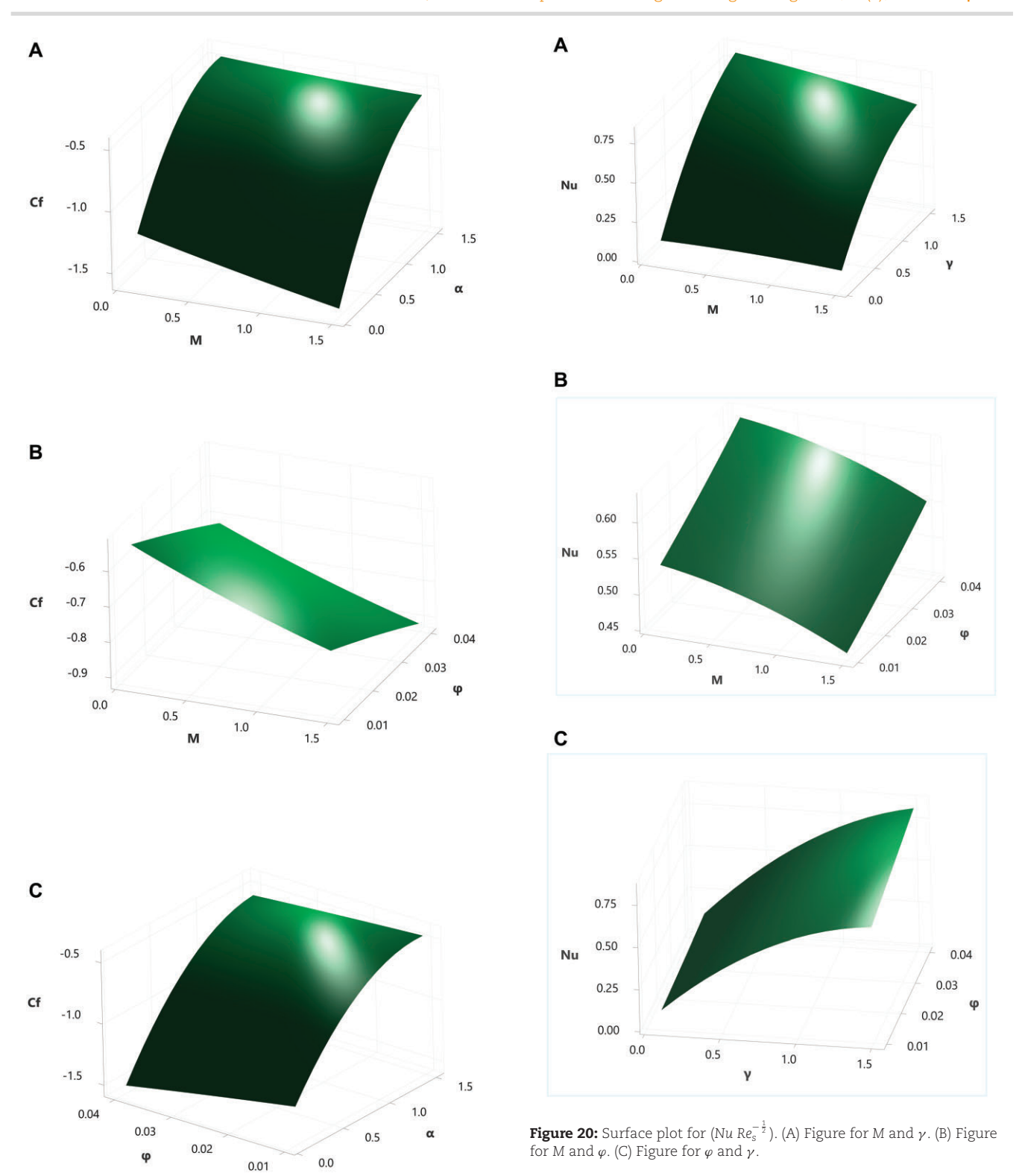


Figure 19: Surface plot for $(C_f Re_s^{\frac{1}{2}})$. (A) Figure for M and α . (B) Figure for M and φ . (C) Figure for φ and α .

most sensitive for the provided values is shown by the highest bar. Figures 21A-C illustrate the sensitivity of the skin friction when the Hartmann values are low. It is observed that the slip parameter has positive sensitivity for medium and low values. It concludes that the slip parameter gradually decreases sensitivity from lower to higher values. The sensitivity of skin friction is illustrated in Figures 21D-F for the intermediate values of the Hartmann number. It is observed that the slip parameter has positive sensitivity for medium and low values, while Hartmann number and volume fraction has negative sensitivity. For high Hartmann numbers, Figures 21G-I show the skin friction sensitivity. All values of the slip parameter are found to have positive sensitivity. It concludes that the slip parameter gradually decreases the magnitude of sensitivity from lower to higher values. These show that, in

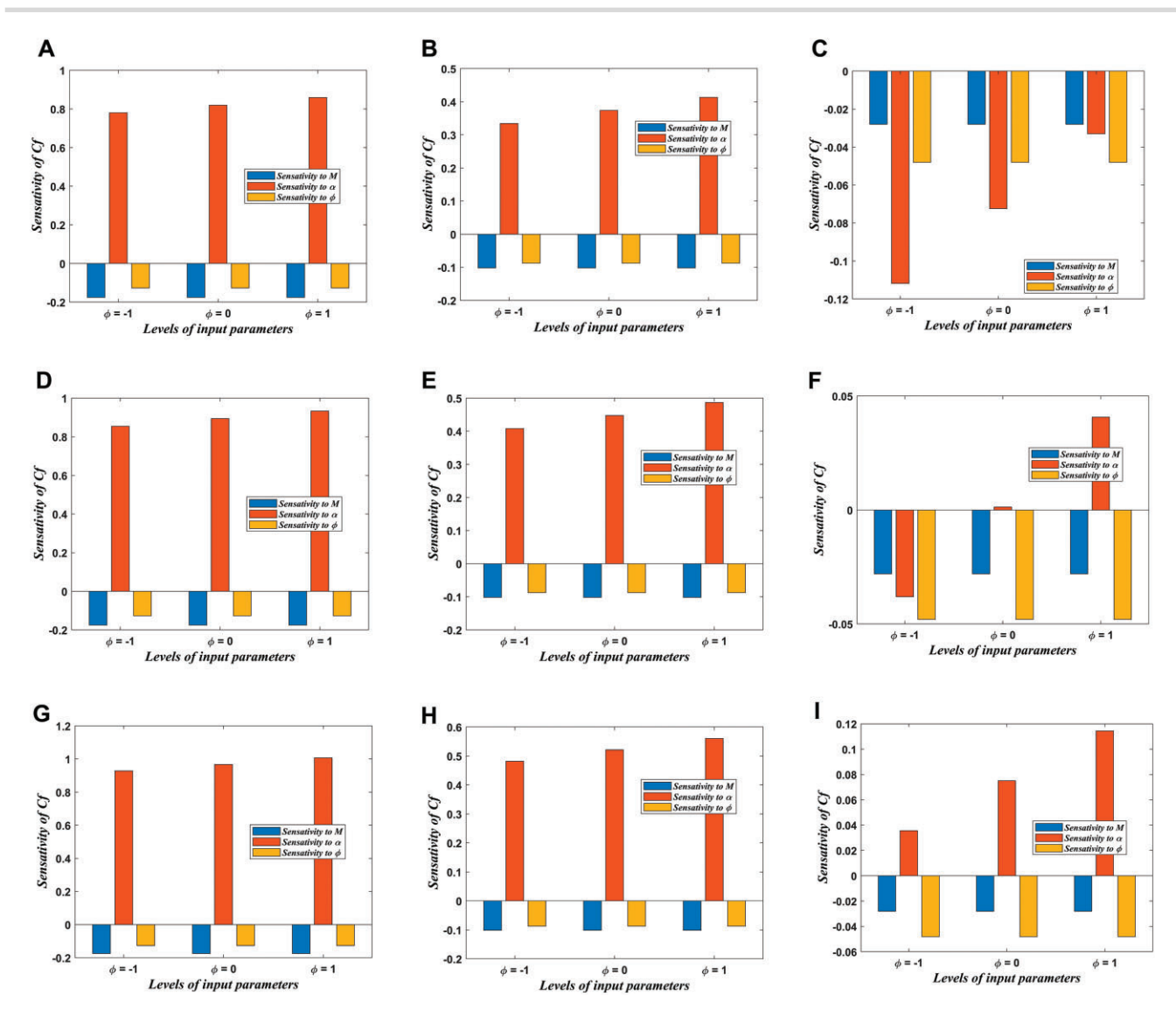


Figure 21: Sensitivity analysis of skin friction for each case. (A) M = -1, $\alpha = -1$. (B) M = -1, $\alpha = 0$. (C) M = -1, $\alpha = 1$. (D) M = 0, $\alpha = -1$. (D) M = 0, $\alpha = -1$. -1. (E) M = 0, α = 0. (F) M = 0, α = 1. (G) M = 1, α = -1. (h) M = 1, α = 0. (i) M = 1, α = 1.

comparison to the volume fraction coefficients and Hartmann number, the slip parameter is the most sensitive. A sensitivity analysis of the Nusselt number for low Hartmann values is presented in Figures 22A-C. There is a positive correlation between the Biot number and volume fraction for small Hartmann number. It concludes that the Biot number is gradually decreasing while volume fraction increases sensitivity. Figures 22D-F show the Nusselt number's sensitivity for the Hartmann number's middle values. The Biot number and volume fraction show positive sensitivity for all values; however, the Hartmann number and volume fraction are negative. The Nusselt number becomes quite sensitive for rising values of Hartmann number, as seen in Figures 22G-I. The Biot number and volume fraction are found to be positively sensitive to all values. It concludes that the slip parameter gradually decreases the magnitude of sensitivity, while volume fraction increases the sensitivity with increasing values of the slip parameter. From these figures, it is observed that the Biot number is most sensitive as compared to Hartmann number and volume fraction coefficients. Furthermore, increasing values of the Biot number sensitivity are reduced with an increment of the Biot number, while volume fraction increases the sensitivity.

8. Conclusion

The RSM and ANOVA are used to optimize the skin friction $(C_f Re_s^{\frac{1}{2}})$ and Nusselt number (Nu $Re_s^{-\frac{1}{2}}$) due to ternary nanofluids past a curved stretching surface with viscous dissipation and magnetic field. We also perform sensitivity analysis for the $(C_f Re_s^{\frac{1}{2}})$ and (Nu Re $_{\rm s}^{-\frac{1}{2}}$). Irreversibility analysis is discussed in detail that arises from Joule heating and viscous dissipation. The modelled equations are transformed into the coupled ODEs by utilizing a non-similar approach. The Bvp4c built-in function is used to obtain the numerical solution. RSM has been utilized to build a correlation between input parameters and output responses. Moreover, residual errors and coefficient regression are computed using ANOVA. Sensitivity analysis of various input factors on output responses is conducted using these numerical and statistical data.

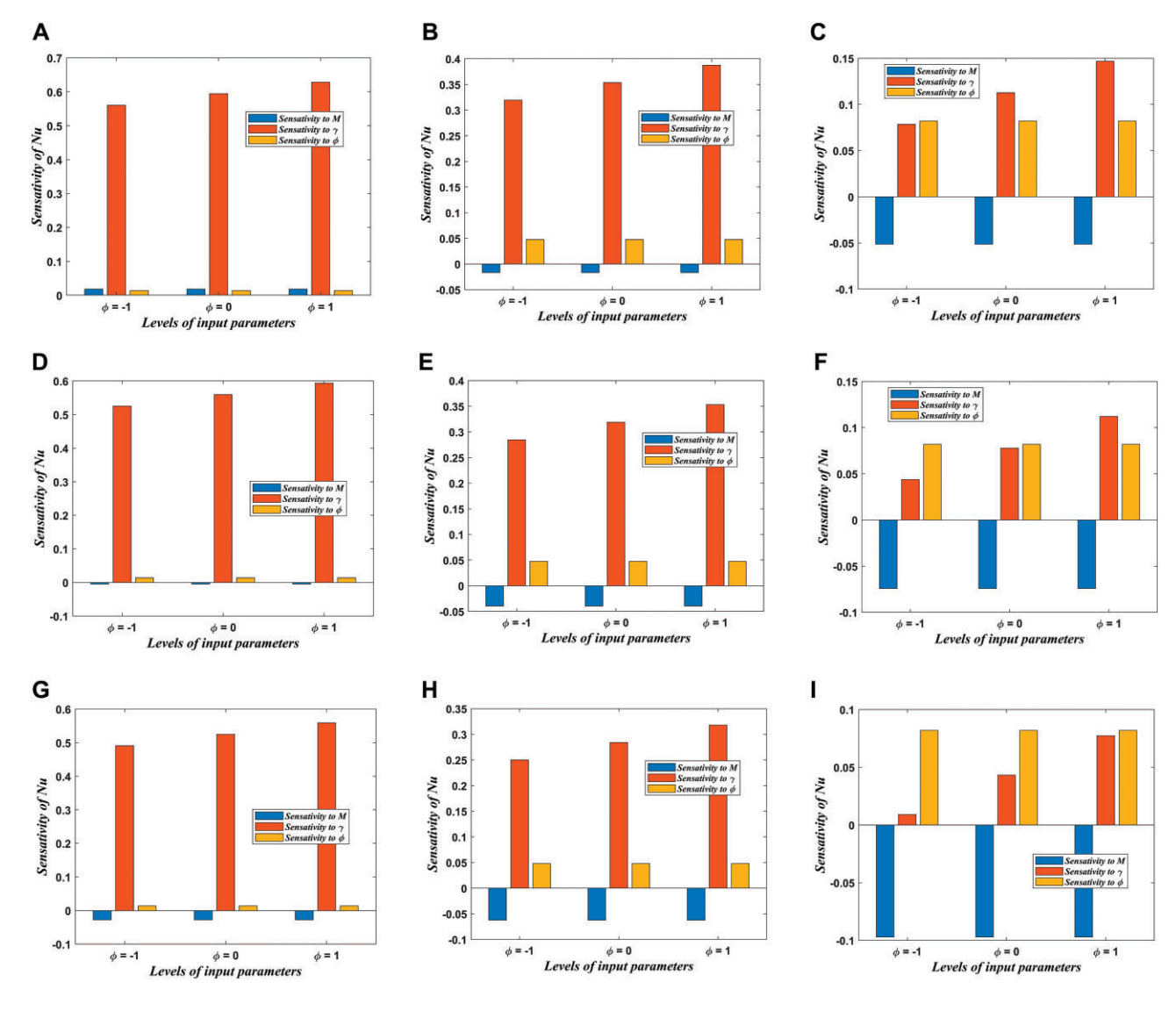


Figure 22: Sensitivity analysis of Nusselt number for each case. (A) M = -1, $\gamma_1 = -1$. (B) M = -1, $\gamma_1 = 0$. (C) M = -1, $\gamma_1 = 1$. (D) M = 0, $\gamma_1 = -1$. (E) M = 0, $\gamma_1 = 0$. (F) M = 0, $\gamma_1 = 1$. (G) M = 1, $\gamma_1 = -1$. (H) M = 1, $\gamma_1 = 0$. (I) M = 1, $\gamma_1 = 1$.

- A higher amount of volume fraction of ternary nanofluids causes the fluid's velocity and temperature to rise.
- The rising volume fraction values of ternary nanofluids increase entropy generation and reduce the Bejan number.
- The slip parameter's rising value decreases fluid velocity.
- The high values of $R^2 = 99.84\%$, $R^2(Adj) = 99.70\%$ for drag force and $R^2 = 99.97\%$, $R^2(Adj) = 99.94\%$ for heat transfer rate show that a strong correlation occurs between input parameters and responses.
- The slip parameter is the most sensitive parameter as compared to Hartmann number and volume fraction for skin fric-
- The Biot number is the most influential parameter as compared to the Hartmann number and volume fraction for heat transfer rate.

8.1. Future work

This work could extend to three dimensions.

- A non-similar solution can be found for a non-Newtonian fluid over a curved stretching surface.
- We could use an unsupervised machine learning algorithm to predict the better solution.
- Stability analysis can be performed on flow over a curved surface.

Conflict of Interest

The authors declare that they have no known competing financial interests or personal relationships that could have appeared to influence the work reported in this paper.

Author Contributions

Sami Ul Haq: Conceptualization, investigation, methodology, visualization, writing-original draft, writing-review & editing. Muhammad Bilal Ashraf: Conceptualization, formal Analysis, supervision. Arooj Tanveer: Validation, visualization, review & editing. Jong-Suk Ro: Formal analysis, data curation, project administration. Fuad A. Awwad: Official analysis, methodology, project administration. Emad A. A. Ismail: Official analysis, data collection, project administration.

Data Availability

Data sets generated during the current study are available from the corresponding author on reasonable request.

Acknowledgments

Ongoing Research Funding Program (ORF-2025-1060), King Saud University, Riyadh, Saudi Arabia. This work was supported by the Korea Institute of Energy Technology Evaluation and Planning (KETEP) and the Ministry of Trade, Industry & Energy (MOTIE) of the Republic of Korea (no. 20214000000280).

References

- Akbar, A. A., Awan, A. U., Nadeem, S., Ahammad, N. A., Raza, N., Oreijah, M., & Allahyani, S. A. (2024). Heat transfer analysis of Carreau-Yasuda nanofluid flow with variable thermal conductivity and quadratic convection. Journal of Computational Design and Engineering, 11, 99-109. https://doi.org/10.1093/jcde/qwae009.
- Alahmadi, R. A., Raza, J., Mushtaq, T., Abdelmohsen, S. a. M., Gorji, M. R., & Hassan, A. M. (2023). Optimization of MHD flow of radiative micropolar nanofluid in a channel by RSM: Sensitivity analysis. Mathematics, 11, 939. https://doi.org/10.3390/math11040939.
- Aldandani, M., Jan, A., Alsaeed, S. S., & Farooq, U. (2025). Artificial neural network technique for simulation of improved thermal energy of Reiner-Philippoff nanofluid over a stretching curved surface. Journal of Computational Design and Engineering, 12, 73–91. https://doi.org/10.1093/jcde/qwaf008.
- Alkinidri, M., Iqbal, J., & Abbasi, F. M. (2025). Analysis of thermal transport and wall stresses for MHD peristaltic motion of Reiner-Philippoff fluid with viscous dissipation and mixed convection effects. ZAMM-Journal of Applied Mathematics and Mechanics /Zeitschrift Für Angewandte Mathematik Und Mechanik, 105, e202400329. https://doi.org/10.1002/zamm.202400329.
- Algahtani, A. H., Fahmy, H. M., Hasanien, H. M., Tostado-Véliz, M., Alkuhayli, A., & Jurado, F. (2024). Parameters estimation and sensitivity analysis of lithium-ion battery model uncertainty based on osprey optimization algorithm. Energy, 304, 132204. https://do i.org/10.1016/j.energy.2024.132204.
- Alrashdan, M. H. S. (2024). Optimizing average electric power during the charging of Lithium-Ion batteries through the Taguchi method. Transactions of Tianjin University, 30, 152-166. https://do i.org/10.1007/s12209-024-00385-2.
- Aly, E. H., & Pop, I. (2019). MHD flow and heat transfer over a permeable stretching/shrinking sheet in a hybrid nanofluid with a convective boundary condition. International Journal of Numerical Methods for Heat & Fluid Flow, 29, 3012-3038. https://doi.org/10.1 108/hff-12-2018-0794.
- Areekara, S., Sabu, A. S., Mathew, A., Parvathy, K. S., & Wakif, A. (2023). Significance of nanoparticle radius on EMHD Casson nanomaterial flow with non-uniform heat source and second-order velocity slip. Numerical Heat Transfer Part B Fundamentals, 85, 604-621. https://doi.org/10.1080/10407790.2023.2252598.
- Bayareh, M. (2023). An overview of non-Newtonian nanofluid flow in macro- and micro-channels using two-phase schemes. Engineering Analysis with Boundary Elements, 148, 165-175. https://doi.org/ 10.1016/j.enganabound.2022.12.033.

- Devi, R. (2024). Computational analysis of convective heat transfer in ternary nanofluid (Al2O3 + CuO + TiO2/H2O) flowing past a porous stretching sheet with temperature dependent viscosity and viscous dissipation. Journal of Nanofluids, 13, 1063-1071. https://doi.org/10.1166/jon.2024.2197.
- Dwidmuthe, P. D., Dastane, G. G., Mathpati, C. S., & Joshi, J. B. (2020). Study of blood flow in stenosed artery model using computational fluid dynamics and response surface methodology. The Canadian Journal of Chemical Engineering, 99, S820-S837. https://do i.org/10.1002/cjce.23991.
- Esfe, M. H., Esfandeh, S., Motallebi, S. M., & Toghraie, D. (2022). A comprehensive study to predict the rheological behavior of different hybrid nano-lubricants: A novel RSM-based analysis. Colloids and Surfaces a Physicochemical and Engineering Aspects, 646, 128886. https://doi.org/10.1016/j.colsurfa.2022.128886.
- Farooq, U., Liu, H., Basem, A., Fatima, N., Alhushaybari, A., Imran, M., Ali, N. B., & Muhammad, T. (2024). Computational investigation of methanol-based hybrid nanofluid flow over a stretching cylinder with Cattaneo-Christov heat flux. Journal of Computational Design and Engineering, 11, 73-82. https://doi.org/10.1093/jcde/q wae059.
- Fayz-Al-Asad, M., Iqbal, Z., Hasan, M. S., Eljaneid, N. H. E., Sarker, M. M. A., Alhazmi, S. E., Shah, J., Algarni, M. M., Awwad, T. M., & Elnageeb, T. (2024). Computational modelling and simulations to study the thermal enhancement in nanofluid flow in undulating wavy cavity of a cylinder: Finite element analysis. Journal of Computational Design and Engineering, 12, 130-144. https://doi.org/10.1 093/jcde/qwae079.
- Geng, Y., Kitahora, T., Iio, S., Choi, Y. D., & Inagaki, M. (2024). Study on the optimum design of cross flow water turbines using RSM with weighted least squares method. Journal of Physics Conference Series, 2707, 012066. https://doi.org/10.1088/1742-6596/2707/1/012066.
- Haq, S. U., Ashraf, M. B., & Garalleh, H. A. (2024). Non-similar solution of hybrid nanofluids over a curved stretching surface with sensitivity analysis. International Journal of Thermofluids, 24, 100913. https://doi.org/10.1016/j.ijft.2024.100913.
- Haq, S. U., Ashraf, M. B., & Nawaz, R. (2023). Nonsimilar solution of hybrid nanofluid over curved stretching surface with viscous dissipation: A numerical study. Numerical Heat Transfer Part A Applications, 85, 1379-1398. https://doi.org/10.1080/10407782.2023.2202
- Haq, S. U., & Mehmood, S. (2024). Thermal and irreversibility analysis of non-Newtonian fluid within trapezoidal cavity containing heated cylinder. Journal of Taibah University for Science, 18. https: //doi.org/10.1080/16583655.2024.2419696.
- Hossain, A., Molla, M. M., Kamrujjaman, M., Mohebujjaman, M., & Saha, S. C. (2023). MHD mixed convection of non-Newtonian Bingham nanofluid in a wavy enclosure with temperature-dependent thermophysical properties: a sensitivity analysis by response surface methodology. Energies, 16, 4408. https://doi.org/10.3390/en16 114408.
- Hosseinzadeh, K., Mardani, Paikar, M., Hasibi, A., Tavangar, T., Nimafar, M., Ganji, D., & Shafii, M. B. (2022). Investigation of second grade viscoelastic non-Newtonian nanofluid flow on the curve stretching surface in presence of MHD. Results in Engineering, 17, 100838. https://doi.org/10.1016/j.rineng.2022.10
- Iqbal, J., & Abbasi, F. M. (2024). Theoretical investigation of MHD peristalsis of non-Newtonian nanofluid flow under the impacts of temperature-dependent thermal conductivity: Application to biomedical engineering. ZAMM—Journal of Applied Mathematics and Mechanics/Zeitschrift Für Angewandte Mathematik Und Mechanik, 104, e202300724. https://doi.org/10.1002/zamm.202300724.

- Joshi, A., Banerjee, R., & Nidhul, K. (2025). Thermo-hydraulic performance and entropy generation analysis of lithium-ion battery with porous medium for temperature homogeneity. International Journal of Ambient Energy, 46, 2447551. https://doi.org/10.1080/01 430750.2024.2447551.
- Khashi'ie, N. S., Waini, I., Mukhtar, M. F., Zainal, N. A., Hamzah, K. B., Arifin, N. M., & Pop, I. (2022). Response Surface Methodology (RSM) on the hybrid nanofluidflow subject to a vertical and permeable wedge. Nanomaterials, 12, 4016. https://doi.org/10.3390/nano1222 4016
- Li, W., Li, A., Yuen, A. C. Y., Chen, Q., Chen, T. B. Y., De Cachinho Cordeiro, I. M., & Lin, P. (2024). Optimisation of PCM passive cooling efficiency on lithium-ion batteries based on coupled CFD and ANN techniques. Applied Thermal Engineering, 259, 124874. https: //doi.org/10.1016/j.applthermaleng.2024.124874.
- Liao, G., Wang, W., Zhang, F., E, J., Chen, J., & Leng, E. (2022). Thermal performance of lithium-ion battery thermal management system based on nanofluid. Applied Thermal Engineering, 216, 118997. https://doi.org/10.1016/j.applthermaleng.2022.118997.
- Louati, H., Khan, S., Mansoor, M., Hilali, S. O., & Gargouri, A. (2024). Analysis of entropy generation via non-similar numerical approach for magnetohydrodynamics casson fluid flow with Joule heating. Entropy, 26, 702. https://doi.org/10.3390/e260
- Madkhali, H. A., Nawaz, M., Rana, S., Alharbi, S. O., El-Shafay, A., Ali, M. R., & Hendy, A. (2023). Effect of Cattaneo-Christov heat and mass flux in Carreau-Yasuda tri-nanofluid. Case Studies in Thermal Engineering, 53, 103787. https://doi.org/10.1016/j.csite.2023.10378
- Mehmood, S., & Rehman, S. U. (2025). Simulation and accurate prediction of unsteady nonlinear convection flow by artificial neural network using numerical data. Physics of Fluids, 37, 043122. https://doi.org/10.1063/5.0264294.
- Mehmood, S., Rehman, S. U., & Batool, A. (2024). Irreversible effects for SWCNT-MWCNT/water based flow with Coriolis force over rotating frame: A numerical study. ZAMM—Journal of Applied Mathematics and Mechanics /Zeitschrift Für Angewandte Mathematik Und Mechanik, 105, e202400048. https://doi.org/10.1002/zamm.20240
- Mondal, S. K., & Pal, D. (2020). Computational analysis of bioconvective flow of nanofluid containing gyrotactic microorganisms over a nonlinear stretching sheet with variable viscosity using HAM. Journal of Computational Design and Engineering, 7, 251-267. https://doi.org/10.1093/jcde/qwaa021.
- Mustafa, J., Abdullah, M., Ahmad, M. Z., Jamil, B., & Sharifpur, M. (2023). Frictional, thermal, and total entropy generation of two-phase nanofluid turbulent flow in a circular heatsink: A numerical study. Engineering Analysis with Boundary Elements, 150, 44-55. https://doi.org/10.1016/j.enganabound.2023 .01.040.
- Nagaraja, B., Almeida, F., Yousef, A., Kumar, P., Ajaykumar, A., & Al-Mdallal, Q. (2023). Empirical study for Nusselt number optimization for the flow using ANOVA and Taguchi method. Case Studies in Thermal Engineering, 50, 103505. https://doi.org/10.1016/j.csite. 2023.103505.
- Ouyang, Y., Basir, M. F. M., Naganthran, K., & Pop, I. (2024). Dual solutions in Maxwell ternary nanofluid flow with viscous dissipation and velocity slip past a stretching/shrinking sheet. Alexandria Engineering Journal, 105, 437-448. https://doi.org/10.1016/j.aej.2024
- Park, S., Lee, H., Park, C., An, J., & Kim, C. (2025). Optimization using kriging metamodel and CMA-ES to improve temperature uniformity of Electric Vehicle liquid-cooled cylindrical Li-ion battery

- BTMS. Journal of Computational Design and Engineering, 12, 167–178. https://doi.org/10.1093/jcde/qwae113.
- Priyadharsini, M., Gururaj, A. D. M., Ismail, M., & Sheremet, M. (2023). Numerical and sensitivity study on the heat transfer due to bioconvection on unsteady radiative MHD blood flow over a permeable artery with chemical reaction effects. International Communications in Heat and Mass Transfer, 147, 106981. https://doi.org/10.1 016/j.icheatmasstransfer.2023.106981.
- Ramzan, M., Ali, F., Akkurt, N., Saeed, A., Kumam, P., & Galal, A. M. (2023). Computational assesment of Carreau ternary hybrid nanofluid influenced by MHD flow forentropy generation. Journal of Magnetism and Magnetic Materials, 567, 170353. https://doi.org/ 10.1016/j.jmmm.2023.170353.
- Rana, P., Sharma, P. K., Kumar, S., Makkar, V., & Mahanthesh, B. (2023). Multiple solutions and stability analysis in MHD non-Newtonian nanofluid slip flow with convective and passive boundary condition: Heat transfer optimization using RSM-CCD. ZAMM—Journal of Applied Mathematics and Mechanics/Zeitschrift Für Angewandte Mathematik Und Mechanik, **104**, e202200145. https://doi.org/10.100 2/zamm.202200145.
- Rao, S., & Deka, P. (2023). Analysis of MHD bioconvection flow of a hybrid nanofluid containing motile microorganisms over a porous stretching sheet. BioNanoScience, 13, 2134–2150. https://doi.org/10 .1007/s12668-023-01180-4.
- Richa, N., Sharma, B. K., Almohsen, B., & Laroze, D. (2024). Intelligent neuro-computational modelling for MHD nanofluid flow through a curved stretching sheet with entropy optimization: Koo-Kleinstreuer-Li approach. Journal of Computational Design and Engineering, 11, 164–183. https://doi.org/10.1093/jcde/q wae078
- Ul-Haq, S., Tanveer, A., Ashraf, M. B., & Nawaz, R. (2023). Artificial neural network (ANN) analysis of non-similar solution of MHD nanofluid flow past a curved stretching surface. Numerical Heat Transfer Part A Applications, 84, 2399–2422. https://doi.org/10.108 0/10407782.2023.2291125.
- Ullah, F., & Ashraf, M. B. (2024a). Numerical heat transfer analysis of carreau nanofluid flow over curved stretched surface with nonlinear effects and viscous dissipation. International Journal of Thermofluids, 100914. https://doi.org/10.1016/j.ijft.2024.10 0914.
- Ullah, F., & Ashraf, M. B. (2024b). Artificial neural network-based computational heat transfer analysis of Carreau fluid over a rotating cone. Physics of Fluids, 36, 113102. https://doi.org/10.1063/5.0235 645.
- Vahedi, S. M., Ghadi, A. Z., & Valipour, M. S. (2018). Application of response surface methodology in the optimization of Magneto-Hydrodynamic flow around and through a porous circular cylinder. Journal of Mechanics, 34, 695-710. https://doi.org/10.1017/jmec h.2018.1.
- Venkateswarlu, B., Chavan, S., Joo, S. W., & Metwally, A. S. M. (2025). Numerical study on cooling enhancement in lithium-ion battery modules using hybrid nanoliquids in flow channels. International Journal of Hydrogen Energy, 112, 231-242. https://doi.org/10.1016/j. ijhydene.2025.02.399.
- Wang, F., Sajid, T., Katbar, N. M., Jamshed, W., Eid, M. R., Abd-Elmonem, A., & El Din, S. M. (2023). Computational examination of non-Darcian flow of radiative ternary hybridity Casson nanoliquid through moving rotary cone. Journal of Computational Design and Engineering, 10, 1657–1676. https://doi.org/10.1093/jcde
- Xiong, Y., Lu, B., Song, Y., & Zhang, J. (2024). Analysis of thermal management and anti-mechanical abuse of multi-functional battery modules based on magneto-sensitive shear thickening fluid. Ap-

- plied Mathematics and Mechanics, 45, 529-542. https://doi.org/10.1 007/s10483-024-3094-8.
- Yang, Z., Gu, J., Luo, X., Qin, Z., Zhou, S., Wang, P., & Zhao, W. (2023). An RSM approach to optimize the thermal performance of novel type vortex generators. Progress in Nuclear Energy, 167, 104978. https: //doi.org/10.1016/j.pnucene.2023.104978.
- Zeng, Z., Yuan, N., Song, C., Liu, J., Liu, Z., & Shi, H. (2025). Integrating CFD and data-driven techniques for the optimization of dielectric coolants in EV battery immersion cooling systems. International Communications in Heat and Mass Transfer, 162, 108591. https://doi. org/10.1016/j.icheatmasstransfer.2025.108591.
- Zhang, L., Zhang, H., Wang, S., Song, J., Yao, X., & Wang, W. (2024). Boundary layer and entropy analysis of non-Newtonian Casson nanofluids moving nonlinearly in a wedge-shaped stretching plate under an unsteady flow. Case Studies in Thermal Engineering, 56, 104193. https://doi.org/10.1016/j.csite.2024.104193.
- Zhang, X., Abidi, A., Ahmed, A. E., Khan, M. R., El-Shorbagy, M., Shutaywi, M., Issakhov, A., & Galal, A. M. (2021). MHD stagnation point flow of nanofluid over a curved stretching/shrinking surface subject to the influence of Joule heating and convective condition. Case Studies in Thermal Engineering, 26, 101184. https: //doi.org/10.1016/j.csite.2021.101184.